GROWTH AND CHARACTERIZATION OF $(InGa)_2O_3$ ALLOYS

by

Brian Samuels, B.S.

A thesis submitted to the Graduate Council of
Texas State University in partial fulfillment
of the requirements for the degree of
Master of Science
with a Major in Engineering
August 2018

Committee Members:

Ravi Droopad, Chair

Larry Larson, Co-Chair

Maggie Chen

FAIR USE AND AUTHOR'S PERMISSION STATEMENT

Fair Use

Duplication Permission

ACKNOWLEDGEMENTS

First, I would like to express my sincere gratitude towards Dr. Ravi Droopad for the opportunity to join his research group, for being my research advisor, and providing an excellent lab facility for me to conduct my research. His guidance and advice have proven invaluable in the completion of my graduate degree.

I would also like to thank the members of Dr. Droopad's research group Khem Baral, Dalim Mia, Sneha Kawal, and Zachary Fox for their help and assistance with various measurements and analysis.

In addition, I would like to thank the rest of my thesis committee. Dr. Larry Larson and Dr. Maggie Chen for their valuable suggestions and assistance.

Lastly, I would like to thank my family for all their support over the years.

TABLE OF CONTENTS

Page

LIST OF TABLES

Table **Page**

LIST OF FIGURES

Figure **Page**

ABSTRACT

To create the next generation of power devices, new materials are being developed for use as wide bandgap semiconductors. Wide bandgap oxides are receiving attention as their properties are conducive to improved power and high breakdown devices. The indium gallium oxide alloy makes it one of the candidates that can be used in heterostructures in which the electrical and optical properties can be tuned. While research has been concentrated on the development and understanding of the properties of In_2O_3 and Ga_2O_3 thin films, there is a need to develop an understanding of the structure and behavior of alloys composed of these metal oxides. This research demonstrates the growth of the cubic form of $(In_xGa_{1-x})_2O_3$ for x = 0.6, 0.8, and 1.0 on sapphire (0001) substrates using pulsed laser deposition. Single crystal films are identified by peaks corresponding to the (222) and (444) planes using high-resolution x-ray diffraction. The optical constants (n, k) are found to be between 1.9-2.0 and 0.0005-0.5 respectively using spectroscopic ellipsometry. The bandgap of the alloys is shown to be 3.68-3.86 eV, with the increase due to an increased gallium composition. Mobility and resistivity of the alloys are $\sim 10^{19}$-10^{20} $cm^2/V^{-1}s^{-1}$ and $\sim 10^{-3}$-10^{-2} $\Omega \cdot cm$ respectively and vary as a result of partial oxygen pressure during growth. This high carrier concentrations with wide bandgap also makes this material useful for transparent conductors and UV applications.

I. INTRODUCTION

Wide bandgap semiconductors are currently being researched to develop the next generation of power devices and opto-electronic devices [1]–[3]. Traditionally, many power converters have been based on silicon (Si) but with limited voltage and current operation. Power devices based on wide bandgap semiconductors such as silicon carbide (SiC) and gallium nitride (GaN) have been demonstrated to operate with higher efficiency, voltages, and frequency than the traditional Si devices [3], [4]. Gallium oxide (Ga_2O_3) has been another wide bandgap (~4.9 eV) semiconductor being developed for power devices since it is predicted to result in improved device performance [5]. The next step in the development of this material system is the fabrication of heterostructures for bandgap engineering needed to tune the electrical and optical properties of the system. To this end, the examination of indium gallium oxide ($(InGa)_2O_3$) as a wide bandgap semiconductor in device heterostructure is required.

Wide bandgap semiconducting oxides are also being considered for UV optoelectronics. Opto-electronic devices have been studied for over 100 years, with the first light-emitting diode (LED) demonstrated by H. J. Round in 1907 using a SiC crystal [6]. Due to the relationship between bandgap and wavelength, several semiconductors have been developed for LEDs and photodetectors. Recently, the Nobel Prize was awarded for the development of an efficient blue LED using GaN [7]. Research continues with other wide bandgap semiconductors moving into the deep-ultraviolet (DUV) wavelength using Ga_2O_3 and related alloys [8]. The development of opto-electronic devices utilizing these alloys will be important for UV emitters and detectors.

1.1 Literature Review

1.1.1 Crystal Structure of In_2O_3

Indium oxide (In_2O_3) exists in several different polymorphs with the stable forms being cubic bixbyite ($Ia\bar{3}$, no. 206) and rhombohedral ($R\bar{3}c$, no. 167) [9]. In addition to these polymorphs, the orthorhombic (*Pbcn*, no. 60) phase is obtained under high-pressure high-temperature conditions (8-9 GPa, 600-1100 °C) but partially decomposes into the rhombohedral phase at ambient pressure [10]. The crystal structure parameters for these phases are shown in Table 1. The focus of this research will be on the cubic phase of In_2O_3 and its alloy with Ga.

The cubic structure of In_2O_3 has a lattice parameter of 10.1170 Å with two types of indium atoms and one type of oxygen atom occupying the 8b, 24d, and 48e Wyckoff positions respectively [11]. The two different indium sites are referred to as the b and d sites in which indium atoms reside in the center of a distorted cube with six corners

Table 1: Lattice and positional parameters for different phases of In_2O_3 [11].

Compound and space group	**Unit cell (Å)**	**Atom**	**Wyckoff site**	***x***	***y***	***z***
c-In_2O_3	a = 10.1170	In1	8b	0.25000	0.25000	0.25000
$Ia\bar{3}$	a = 10.1170	In2	24d	0.46650	0.000	0.25000
	a = 10.1170	O	48e	0.39085	0.15435	0.38140
rh-In_2O_3	a = b=5.4814	In	12c	0.0000	0.000	0.35720
$R\bar{3}c$	c = 14.4998	O	18e	0.96367	0.33333	0.58330
o-In_2O_3	a = 7.9295	In	8d	0.11483	0.74607	0.02627
Pbcn	b = 5.4821	O1	8d	0.85114	0.61188	0.09552
	c = 5.55898	O2	4c	0.0000	0.03792	0.25000

occupied by oxygen atoms and two corners with oxygen vacancies [12]. In the b site, the vacancies are located diagonally across the cube, whereas the vacancies in the d site are diagonally along a face as shown in figure 1.1. The unit cell contains 80 atoms which include 8 and 24 of these b and d site cations respectively [13].

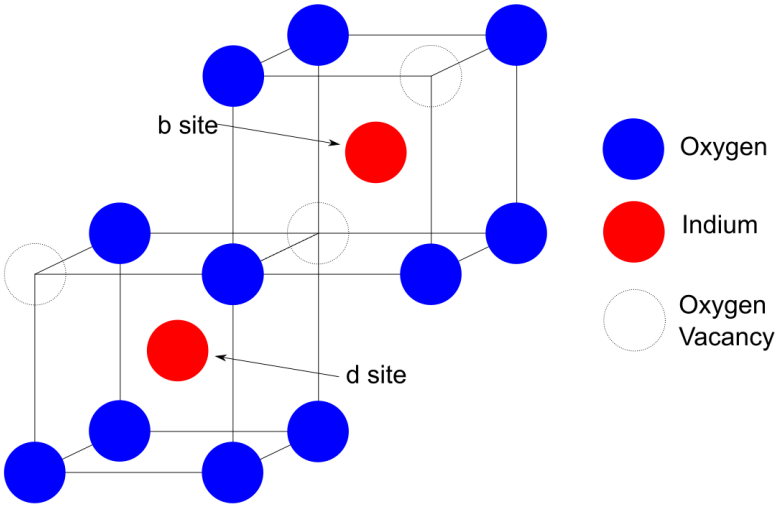

Figure 1.1: Crystal structure of cubic bixbyite In_2O_3 with the b and d sites.

1.1.2 Crystal Structure of Ga_2O_3

Gallium oxide (Ga_2O_3) crystallizes in 5 different polymorphs (α, β, γ, δ, ε) with the monoclinic β-phase being the most stable structure [14]. All other polymorphs are metastable and transform into the β-phase at temperatures between 750-950 °C [15]. Although α-Ga_2O_3 has shown increased stability with the doping of aluminum, the remaining γ-, δ-, and ε-phases are less studied due to poor crystallinity [16]. The lattice parameters of these 5 polymorphs are shown in Table 2.

The monoclinic structure of β-Ga_2O_3 has lattice parameters of 12.23, 3.04, and 5.80 Å for a, b, and c respectively with a lattice angle of β = 103.7 °. This structure

contains two inequivalent Ga positions (Ga(I), Ga(II)) with tetrahedral and octahedral geometries respectively and three positions for the oxygen atoms (O(I), O(II), O(III)).

Table 2: Lattice parameters for polymorphs of Ga_2O_3 (adapted) [14].

Polymorph	**Structure**	**Space group**	**Lattice parameters**
α	rhombohedral	$R\bar{3}c$	a = 4.9825 Å c = 13.433 Å
β	monoclinic	C2/m	a = 12.23 Å b = 3.04 Å c = 5.80 Å β = 103.7 °
γ	cubic	$Fd\bar{3}m$	a = 8.238 Å
δ	body-centered cubic	$Ia\bar{3}$	a = 10.00 Å
ε	orthorhombic	$Pna2_1$	a = 5.120 Å b = 8.792 Å c = 9.410 Å

Figure 1.2 depicts the unit cell of β-Ga_2O_3 along the a-, b-, and c-axis. The bandgap of β-Ga_2O_3 is ~4.9 eV [14]. While this material in its monoclinic phase has important properties for high power devices with large electrical breakdown, its alloys with indium present an important opportunity to expand the application to include tunable bandgap devices in the ultraviolet region. However, the end members of the alloy viz. β-Ga2O3

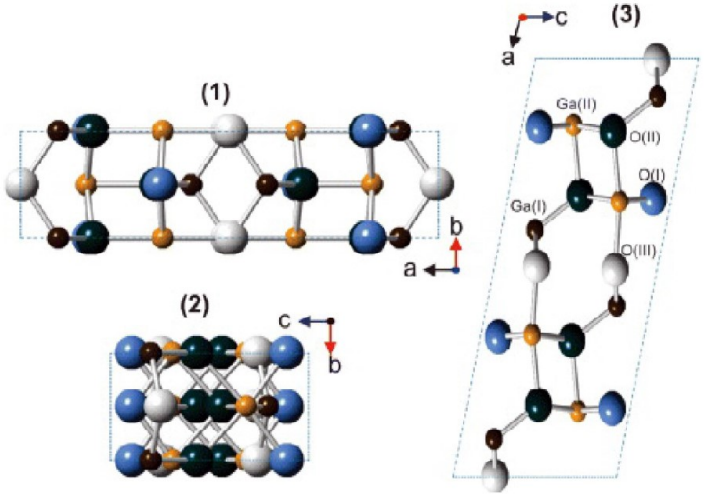

Figure 1.2: Depiction of the unit cell of β-Ga_2O_3 along the c-(1), a-(2) and b-axis [14].

and In_2O_3 have monoclinic and a bixbyite cubic structure respectively with a phase transformation from the monoclinic to cubic structure occurring at indium compositions above 43% as reported by Oshima and Fujita[17]. In this work the focus will be on the cubic structure and properties of $(InGa)_2O_3$ with indium compositions ≥ 60%.

1.1.3 Material Properties of In_2O_3

Indium oxide is a wide bandgap semiconductor with a reported bandgap of 3.7 eV. A comparison of the basic properties with those of Ga_2O_3 is shown in Table 3. In its stoichiometric form, In_2O_3 behaves as an insulator, but, if prepared in oxygen-deficient form, In_2O_3 can reach high n-type doping levels [18]. Carrier concentration is often reported to be between 10^{17} and 10^{20} cm^{-3} where an increased oxygen pressure results in lower carrier concentration [19]. Bierwagen also showed that annealing in O_2 results in an increase in carrier mobility from ~140 up to 230 $cm^2/V{\cdot}s$. Doping levels can be further increased using Ge, W, Mo, and H as dopants, but the most commonly reported high conductivity form of In_2O_3 is indium tin oxide (ITO). Doping with tin has been shown to reduce the resistivity by the addition of free electrons to the conduction band [20]. Kim *et al.* also demonstrated an increase in carrier concentration due to tin doping, with a reduction of the carrier mobility [21]. This reduction in mobility is due to the dopant atoms randomly occupying indium sites within the lattice, thus increasing scattering.

The presence of oxygen vacancies will also influence the transmittance of the film. Kaleemulla *et al.* demonstrated that an increase in oxygen partial pressure during growth will increase the transmittance, saturating at 87 % transmittance at an oxygen

pressure of 2 x10^{-3} mbar [22]. However further increase in pressure shows a reduction in transmittance.

Table 3: Basic properties of In_2O_3 and Ga_2O_3.

	In_2O_3	**Ga_2O_3** [14]
Bandgap (eV)	3.7 [23]	~4.9
Melting point (°C)	1910 [24]	1725
Dielectric constant	8.9 [25]	6.5-7.6
Refractive index	1.6-2 [26]	1.97
Density (g/cm^3)	7.18 [24]	5.95

1.1.4 Growth Methods of In_2O_3

To fabricate In_2O_3 films, various techniques have been used including sputtering [27], atomic layer deposition (ALD) [28], spray pyrolysis [26], [29], chemical-vapor deposition (CVD) [30], metalorganic CVD [31], [32], molecular-beam epitaxy (MBE) [33], and pulsed laser deposition (PLD) [34], [35]. In this research the focus will be on the PLD technique for the growth of single crystal cubic In_2O_3 and its alloys with Ga.

The PLD method has been demonstrated to be a successful method for the growth of crystalline In_2O_3 films. The popularity of this technique is due to the simple operation of the system, as few parameters such as temperature, pressure, laser energy, and pulse rate need to be controlled [35]. In addition, there is a transfer of stoichiometry from the target to the growth film. High-quality films have been produced on a variety of substrates including Si, GaAs, quartz, yttrium stabilized zirconia (YSZ), and sapphire [32]–[35]. Gupta *et al.* demonstrated high-quality thin films of In_2O_3 using PLD under various temperatures (room temperature to 600 °C) and pressures (5.0 x10^{-7} to 1.0 x10^{-5} bar) [34]. This group investigated the structural, optical, and electrical properties of the films and reported that low oxygen pressure during growth favored the formation of higher-quality single crystal films with a preferred orientation along the (222) plane when

grown on sapphire substrates. Also shown was an increase in grain size with an increase in temperature, and a decrease in size with an increase in oxygen pressure. This group also showed an increase in transmittance with an increase in growth temperature with little difference in transmittance due to oxygen partial pressure. They ultimately showed that at a temperature of 400 °C and oxygen pressure of 1.0 $x10^{-6}$ bar in resulted a film with high transparency (~90 %), high mobility (119 $cm^2V^{-1}s^{-1}$), and low resistivity (1.7 $x10^{-4}$ Ω·cm).

Mei *et al.* examined In_2O_3 grown by MBE on sapphire (0001) substrates to determine the relationship between the In_2O_3 (111) and Al_2O_3 (0001) orientations [36]. The group reported that the hexagonally packed indium plane of In_2O_3 (111) is matched in parallel to the close-packed oxygen plane of sapphire (0001) with a rotation of 30 ° from the main lattice. Additionally, they showed the parallel orientations of In_2O_3 ($11\bar{2}$) and sapphire ($11\bar{2}0$) using high-resolution electron microscopy (HREM). Figure 1.3 illustrates the atomic arrangement in In_2O_3 (111) and Al_2O_3 (0001). For this research, growth of $(InGa)_2O_3$ will be conducted using sapphire (0001) substrates.

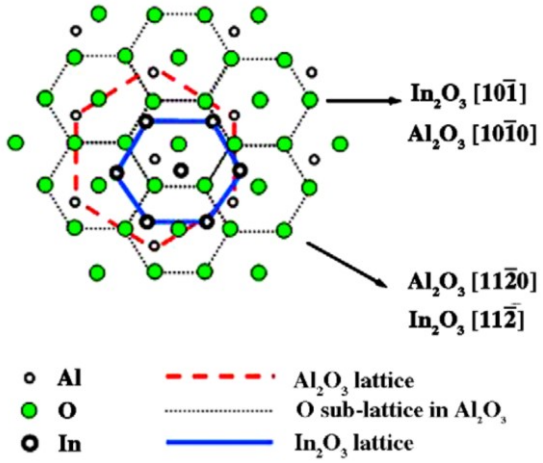

Figure 1.3: Diagram of the atomic arrangement in In_2O_3 (111) and Al_2O_3 (0001) [36].

1.1.5 Alloy of $(In_xGa_{1-x})_2O_3$

The alloy of $(InGa)_2O_3$ is a promising material for semiconductor devices due to the large bandgap range of 3.7 – 4.9 eV covering the wavelength range of 253 – 335 nm. This wavelength range falls within the ultraviolet (UV) spectrum opening the possibility for use of this alloy in UV opto-electronic devices, photodetectors, anti-bacterial light sources, light therapy in medicine, and forensic analysis.

Work presented by Zhang *et al.* has demonstrated $(InGa)_2O_3$ film growth on sapphire (0001) at 500 °C by PLD over a variety of compositions [37]. It was shown that for indium content between 0.16 and 0.33 mixed phases of the cubic and monoclinic structures were produced. With an indium content less than 0.16 only the monoclinic phase appeared in the XRD pattern. An indium content above 0.83 produced the single crystal cubic structures, and for indium content between 0.33 – 0.56 showed polycrystalline cubic structure with XRD peaks representing the (222) and (400) orientations were present. Additionally, optical transmission spectra were measured and indicated a bandgap increasing from 3.8 eV to 5.1 eV corresponding to the increased gallium content from 0 to 100 % respectively.

Oshima and Fujita did a similar study examining the phase separation between cubic In_2O_3 and monoclinic Ga_2O_3 using MBE [17]. All samples in this study were grown by MBE on sapphire (0001) at 800 °C with a buffer layer of monoclinic Ga_2O_3. XRD scans reveal the appearance of cubic In_2O_3 at an indium composition of 43 %, but due to the buffer layer it is unclear at which indium composition the film becomes entirely single crystal cubic. They observed a degradation in crystallinity for high indium composition and low temperature growth was necessary to suppress phase separation.

Transmission spectra was taken for these samples and calculated the bandgap range to be between 4.0 eV and 5.0 eV, increasing with the increase in gallium composition.

Due to the influence of oxygen pressure on the properties of indium oxide discussed earlier, further research is required to determine the structural, optical, and electrical characteristics of these alloys formed in different partial oxygen pressures. In this study, the growth of $(InGa)_2O_3$ with indium composition $\geq$60% will be growth as a function oxygen partial pressure to investigate the crystal structure and electrical and optical properties.

II. GROWTH METHOD AND CHARACTERIZATION TECHNIQUES

2.1 Film Deposition Technique

2.1.1 Pulsed Laser Deposition

Pulsed laser deposition (PLD) is among the physical vapor deposition (PVD) techniques used to deposit thin films using high power laser pulses directed at an elemental or composite source material to transfer the source composition onto a substrate [38]. Development of PLD systems began in the 1960's after the development of the first high-power ruby laser and was demonstrated by Smith and Turner in 1965 to be a viable method for the deposition of thin films [39]. The schematic diagram of a typical PLD chamber is shown in figure 2.1 [40]. The substrate and target are introduced into the growth chamber using a transfer arm from the load lock chamber. The excimer laser is situated externally to the growth chamber and interacts with the target through a transparent port at a 45° angle to the target. The chamber pressure is controlled by the

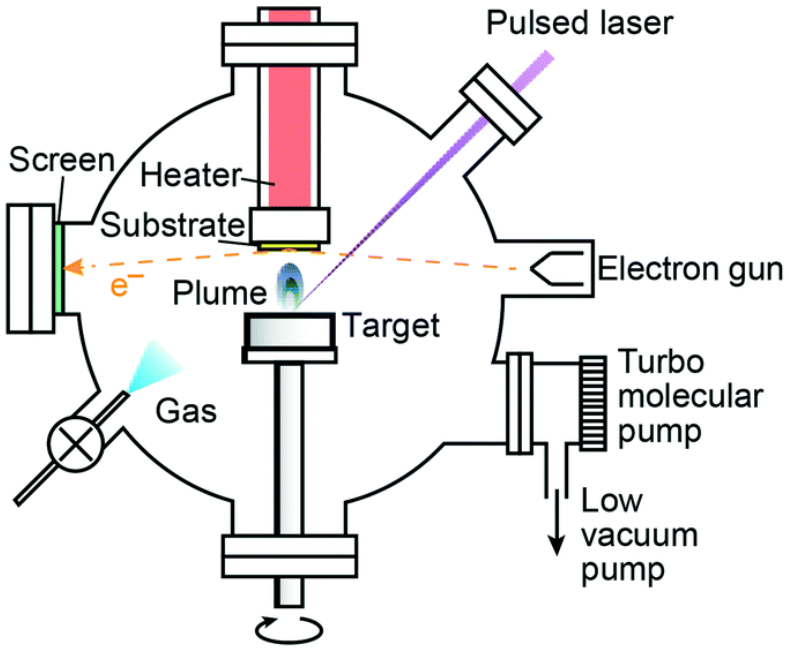

Figure 2.1: Schematic diagram of PLD system [40].

turbo molecular pump and which can achieve a base pressure of ~10^{-9} Torr. However during growth, the pumping speed can be varied (by varying the speed of the turbo pump or by partially closing the gate valve) so that, in combination with the gas flow rate, the pressure in the chamber can be maintained at a constant value during growth. Inlet valves and mass flow controllers allow the controlled introduction of gasses into the chamber during growth to maintain the required stoichiometry of the deposited films. In the system at Texas State University a differentially pumped reflection high energy electron diffraction (RHEED) system is included to allow for the monitoring of the growth surface during in real time.

PLD has several advantages increasing its popularity among researchers. First, the composition of the target can be transferred directly to the deposited film eliminating the need for individual source control to create the desired stoichiometric composition as in MBE (molecular beam epitaxy). The second advantage is the large pressure range (10^{-9} – 10^{-2} Torr) in which deposition can occur. This flexibility allows for the introduction of background gases providing an additional control variable to optimize crystalline and stoichiometry of the films during the growth process. The third advantage is due to the laser being a separate part of the deposition system. Complex multilayer films can be produced with relative ease by manipulating the desired targets into the target position of the beam.

In comparison to other deposition techniques, PLD is a relatively simple method to deposit films. Contained within the chamber are the substrate holder and target holders. The substrate holder contains a radiative heater to control the temperature of the substrate during deposition. A motor is attached to the substrate holder to allow for the

rotation of the substrate to promote uniform deposition. The high-power laser is used as an energy source for the vaporization of the target materials and is directed by lenses through a port into the deposition chamber and onto the surface of the target. The laser beam is typically scanned onto the rotating target to reduce irregular target erosion.

The critical component of the PLD system is the laser, which is selected at a wavelength to optimize absorption into the target material or selected for general purpose to deposit various target materials. The typical operating wavelength of excimer lasers ranges from 200 – 400 nm with examples listed in Table 4. Optical elements are positioned outside the chamber to direct and focus the beam to produce energy densities greater than 1 J/cm^2.

Table 4: Excimer laser wavelengths.

Excimer	**Wavelength (nm)**
F_2	157
KrCl	222
KrF	248
Cl_2	259
XeBr	282
XeCl	308
N_2	337
XeF	351

In this study, a COMPex Pro KrF excimer laser with 248 nm wavelength is used to ablate the material from the target to deposit it onto the substrate, as this is the system available at Texas State University.

2.1.2 Target Preparation

A hard, dense target is required for the deposition of films using PLD. The targets are prepared using a solid state process termed “ceramic sintering”, where a

powder is transformed into a solid, dense ceramic by using heat [41]. This process utilizes high purity oxide powders combined by weight to produce the desired atomic ratio. The powders are mixed using a ball miller for 1 hour to produce a uniform distribution throughout the target. The mixture is placed into a mold and pressed using a heated hydraulic press at a pressure of approximately 19000 lb/in^2 and temperature of 450 °C for a period of 20 hours. The target is then sintered in a tube furnace at 1000 °C in argon gas for 20 hours.

2.2 Structural Characterization

2.2.1 X-ray Diffraction

X-ray diffraction (XRD) is a non-destructive analysis technique used to determine the crystal properties of various materials including liquids, powders, and crystalline films. This technique can reveal information about a material including crystal structure, crystalline quality, orientation, and internal stress [42]. When impacted by the beam of x-rays, an ordered array of atoms within the material cause the radiation to be diffracted. The resulting diffraction pattern, caused by interference, is modeled by Bragg's law which is described by the following equation [43]:

$$n\lambda = 2d \sin\theta. \tag{2.1}$$

In this equation, n is an integer representing the order of the diffraction peaks, λ is the wavelength of the incident radiation, d is the interplanar spacing of the material, and θ is the incident angle between the x-rays and the material. These parameters are shown in figure 2.2. The x-ray source is directed at the sample containing an array of atoms at an incident angle θ. The incident beams reflect from the parallel planes and, due to the difference in path length, exhibit a phase difference. Constructive interference occurs

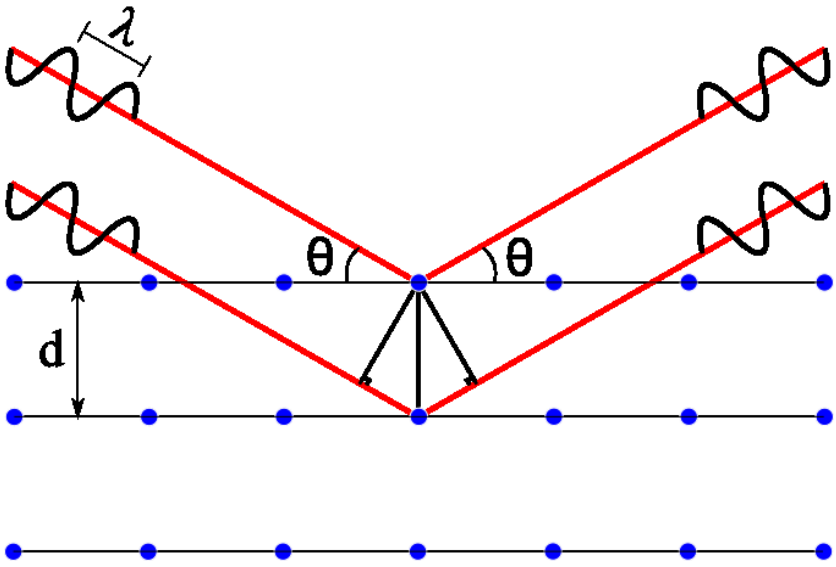

Figure 2.2: Schematic diagram representing Bragg's law.

when the difference in path lengths is equal to a multiple integer of the wavelength [42]. The diffracted rays are measured for intensity typically plotted versus 2θ where θ is the incedent angle of the X-ray beam as illustrated in Fig.2.2. The resulting spectrum is analyzed by comparison to the database of known crystalline materials to identify the orientation(s) within the material.

2.2.2 X-ray Photoelectron Spectroscopy

In X-ray Photoelectron Spectroscopy (XPS), the surface of a sample is analyzed to reveal information on bonding configurations, elemental composition, and band structure of the surface atoms exposed to an X-ray beam. This is achieved by the irradiation of the surface by Al Kα (1486.6 eV) or Mg Kα (1253.6 eV) x-rays. The interaction between the radiation and the core electrons results in the ejections of photoelectrons from the electronic shell due to the collision between x-rays and electrons [44]. The kinetic energy of these photoelectrons collected by the photodetector can be approximated as the difference between the photon energy of the radiation and the

binding energies of the ejected electrons from the shell. This binding energy E_b is given by

$$E_b = h\nu - E_k - \phi_A \qquad 2.2$$

where hν is the characteristic energy of the x-ray, E_k is the kinetic energy of the ejected electron, and ϕ_A is the work function of the analyzer [45]. A schematic of the photoelectron emission process is shown in figure 2.3 together with a typical XPS spectrum [44]. Also present in the spectrum are signatures of Auger electrons that are generated when an electron from valence shell filled the hole caused by the missing inner core electron in the electronic shell in a process to conserve energy.

To the measured XPS spectrum is analyzed to determine the elements with other relevant properties of the sample, in this study the oxidation states of the cations are determined as a function of the growth conditions and used to correlate the electrical and optical properties of the thin films. The change in the binding energy representing the differences in the chemical bonding is used to extract information about the oxidation or chemical state of the elements in the sample [46].

The XPS measurements were carried out using Scienta analyzer and with an Al Kα (1486.6 eV) radiation from a Specs dual anode source. The samples were removed from the PLD chamber and transported in air to the XPS chamber resulting in a C peak that can be used to correct for any charging due to inadequate grounding of the sample. To analyze the data, a Shirley background is used to fit the measured data and acquired peaks with a deconvolution of obtained spectra that were carried out by the summation of Gaussian line shapes that define individual components of the measured peaks from which information of the chemical interactions properties of the elements can be extracted.

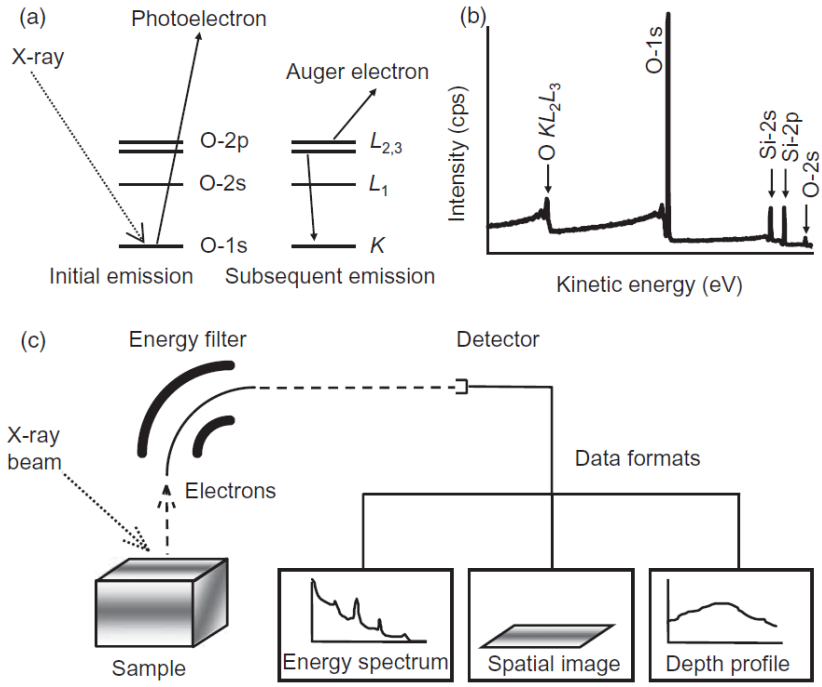

Figure 2.3: Schematic diagram of (a) the photoelectron and Auger de-excitation process, (b) an example of the collected XPS spectra, and (c) the basic components of an XPS system [44].

2.3 Optical Characterization

2.3.1 Spectroscopic Ellipsometry

Ellipsometry is an optical measurement technique used to indirectly determine the optical constants, thickness, and roughness of single or multiple layer films. This technique measures the change in polarized light reflected from a sample which often becomes 'elliptical' [47]. There are two main sections of an ellipsometer consisting of a polarization state generator (PSG) and polarization state detector (PSD) which are shown in figure 2.5 [48]. The PSG consists of the light source and optical elements to produce a known polarization state with parallel (p) and perpendicular (s) components. The light reflects on the sample surface toward the optical components and detector within the PSD which determines the new polarization state.

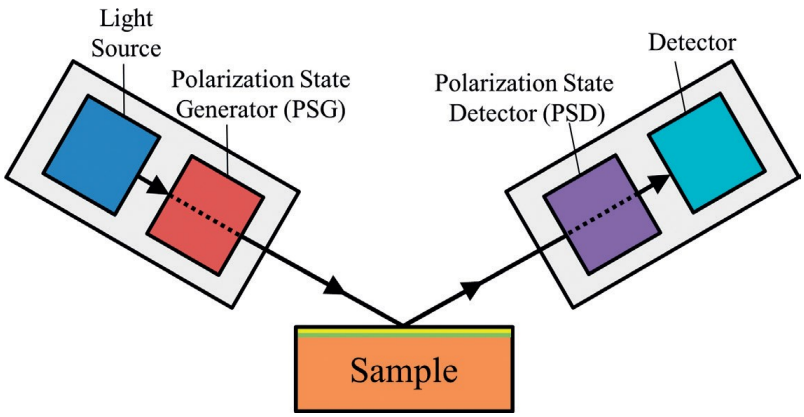

Figure 2.4: Schematic diagram of ellipsometry [48].

Two values are measured using ellipsometry: the amplitude ratio ψ and phase difference Δ between p- and s-polarized light [48]. These values (ψ, Δ) are defined by the complex reflectance ratio ρ as

$$\rho = \tan(\psi)\exp(i\Delta) = \frac{r_p}{r_s} \qquad 2.3$$

where r_p and r_s are the amplitude reflection coefficients for the parallel and perpendicular components respectively [49]. To determine the thickness and optical constants, a model must be developed and fitted to ψ and Δ over a range of wavelengths. This model, based on Fresnel's equation, is compared with the measured values using an estimator like the mean squared error (MSE) and the unknown variables of the model are varied until the lowest MSE is achieved. The formula defining MSE is defined as

$$MSE = \sqrt{\frac{1}{3n-m}\sum_{i=1}^{n}[(N_{E_i} - N_{G_i})^2 + (C_{E_i} - C_{G_i})^2 + (S_{E_i} - S_{G_i})^2] \times 1000} \qquad 2.4$$

where m is the number of fitting parameters, n is the number of wavelengths, C=sin(2ψ)cos(Δ), S=sin(2ψ)sin(Δ), N=cos(2ψ), and the subscripts E and G represent the measured and generated parameters respectively.

2.3.2 UV-Vis Spectroscopy

Ultraviolet-visible spectroscopy is a technique used to measure the absorption or transmittance of the electromagnetic spectrum in the ultraviolet to visible to near infrared wavelengths. This method utilizes a pair of emitters and detectors for a wavelength range between 200-900 nm. One emitter/detector pair passes light through the sample while the other pair passes light through a reference substrate, or through air. In this study, a sapphire substrate is used as reference for the measurements. The measurements from the detectors are compared to determine the transmittance of the film.

The bandgap can also be calculated from the transmittance data collected from the measurements. Absorption of the film follows the power law

$$(\alpha hv) = B(hv - E_g)^{1/2} \qquad 2.5$$

where α = Absorption/wavelength, B is the absorption edge width parameter, hv is the energy of the photon, and E_g is the bandgap [50].

2.4 Electrical Characterization

2.4.1 Measurements

Hall measurement is a method used to determine the electrical characteristics of a material including: sheet resistance, resistivity, mobility, and carrier concentration. The van der Pauw technique is widely used in industry due to the ease and convenience of the geometry [51]. Figure 2.5 illustrates the van der Pauw geometry used for this research.

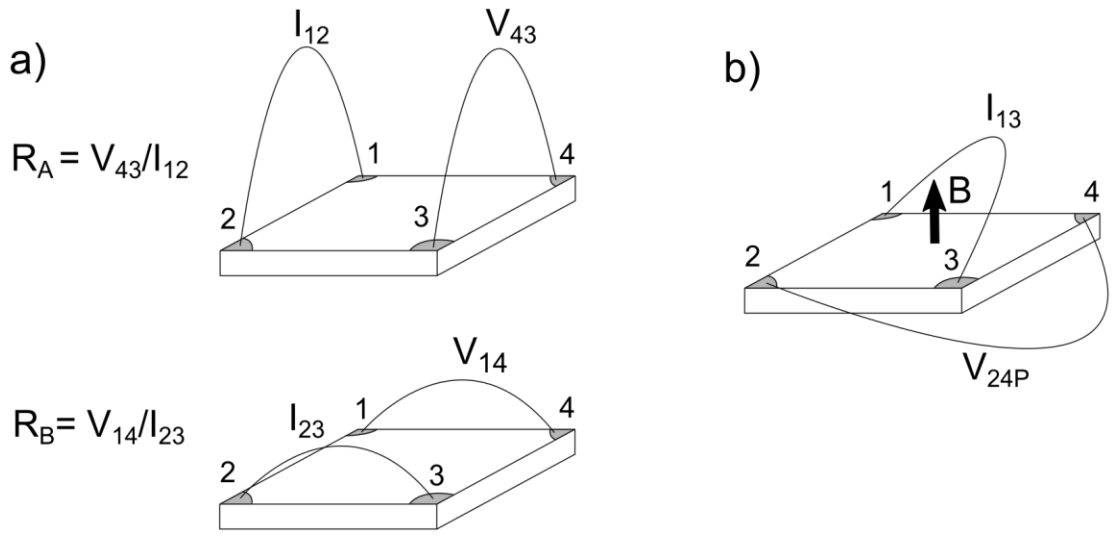

Figure 2.5: Illustration of the sample geometry for van der Pauw (a) resistivity and (b) Hall measurements (adapted) [51].

Resistance measurements (R_A, R_B) are taken according to the equations shown in fiqure 2.5(a). Reciprocal measurements of R_A and R_B are averaged to obtain a more precise value for the two characteristic resistances and renamed as R_V and R_H. For additional refinement of the measurement, the voltage and current contacts are switched, and the characteristic resistances are found by the average of the four resistance measurements. The relationship between the sheet resistance (R_S) and two characteristic resistances is shown by the van der Pauw equation

$$exp\left(-\pi {R_V}/{R_S}\right) + exp\left(-\pi {R_H}/{R_S}\right) = 1. \quad 2.6$$

Solving this equation for R_S, the resistivity (ρ) can be found by

$$\rho = R_S d \quad 2.7$$

where d is the thickness of the sample.

To calculate the Hall voltage, the configuration shown in figure 2.5(b) is used. A constant current (I_{13}) is applied and the voltage (V_{24P}) is measured while a constant

positive (subscript P) or negative (subscript N) magnetic field (B) is applied perpendicular to the sample. The current I_{13} is a positive current produced between contact 1 and contact 3 while the voltage V_{24} is the voltage difference across those contacts (V_4 - V_2). The net voltage for each measurement (the difference between the measured voltage with a positive and negative magnetic field (e.g., $V_{24} = V_{24P} - V_{24N}$)), is then averaged to give the Hall voltage (V_H). With the Hall voltage known, the carrier concentration (n) can be derived using the equation

$$n = \frac{IB}{q|V_H|} \tag{2.8}$$

Upon finding the sheet resistance and carrier concentration, the mobility (μ) of an n-type semiconductor can be found by

$$\mu = \frac{1}{qnR_s} \tag{2.9}$$

where q = -1.602 x10^{-19} C.

2.4.2 Transmission Line Measurements

Transmission line measurements (TLM) are utilized to determine the resistance of metal contacts, sheet resistance, and contact resistivity. The contacts, consisting of a length L and width W, are arranged in parallel with an increase in spacing (d) from one contact to the next. Figure 2.6(a) shows the layout of a TLM test structure. I-V measurements are taken for each pair of adjacent contacts across each distance. The resistance (calculated using Ohm's law, V=IR) is then plotted as a function of the spacing (d) between the measured contacts. An example of this plot is displayed in figure 2.6(b) [52]. From this plot, a linear fit model is applied to the data points. From this line, the

sheet resistance (R_{SH}), contact resistance (R_C), and transfer length (L_T) can be extrapolated. The contact resistivity (ρ_c) can then be calculated using

$$\rho_c = R_C L_T W. \tag{2.9}$$

In this study contacts were fabricated using a photolithography process where metal is deposited using electron beam evaporation onto a lift-off resist, then removed with solvents to expose the pattern.

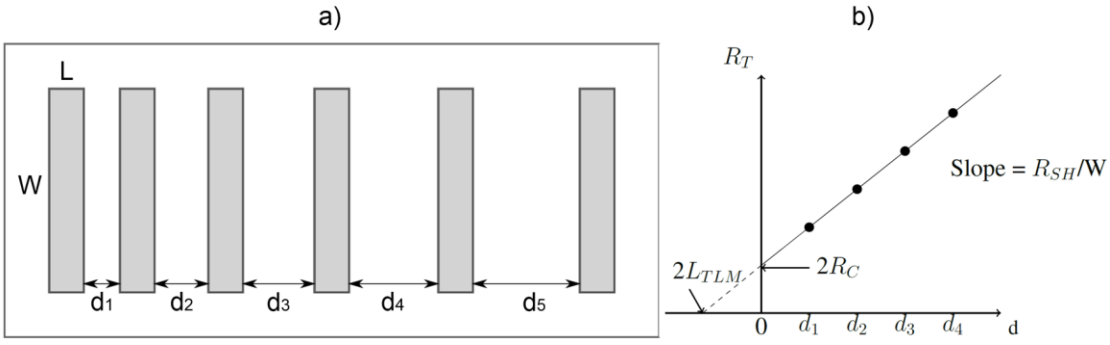

Figure 2.6: Schematic diagram of TLM structure (a), and an example of the resistance vs. contact distance plot (b) [52].

III. GROWTH AND CHARACTERIZATION OF $(InGa)_2O_3$ FILMS

3.1 Film Growth

3.1.1 Experimental

The growth of films using the PLD process begins with the fabrication of the oxide targets. The targets are prepared using high-purity (99.999 %) powders with different indium content with the molar ratios of In/(In + Ga) equaling 0.6, 0.8, and 1.0. For growth of $(In_xGa_{1-x})_2O_3$ films, the base pressure of the chamber is set to ~10^{-6} Torr using a turbomolecular pump set to 170 Hz. Two-inch diameter single-side polished c-plane sapphire wafers are prepared by ultrasonically cleaning with organic solvents (acetone, isopropanol) followed by a deionized water rinse and dried with nitrogen gas. Once loaded into the chamber through the load lock the wafer is heated to a fixed growth temperature of 400 °C and placed at a distance of 5 cm above the target. While 400 °C was determined to be an ideal growth temperature for In_2O_3, in this study no attempts were made to optimize the temperature for the alloy growth containing gallium. Both substrate and target undergo rotation during the growth process to aid in uniform film growth. A KrF excimer laser (λ = 248 nm) was used as the energy source with the energy set to 300 mJ at a pulse rate of 10 Hz. The growth for all the layers were set for 18000 laser pulses or 30 mins. Oxygen is introduced into the chamber and the films growth for various flow rates of 0, 300, 450, 600, 750, and 900 sccm equating to chamber pressures of 4.6 x10^{-6}, 8.5 x10^{-3}, 1.6 x10^{-2}, 2.5 x10^{-2}, 4.1 x10^{-2}, and 7.5 x10^{-2} Torr respectively. After deposition the substrate is cooled at a rate of 5 deg./min and the oxygen flow stopped once the substrate temperature reaches below 300 °C.

3.1.2 Results and Discussion

XRD diffraction is used to determine the crystalline properties of the grown films. The two theta-omega (2θ-ω) XRD scan of $(In_xGa_{1-x})_2O_3$ thin films grown on sapphire is shown in figure 3.1 for various levels of indium content (x). The films are grown at a substrate temperature of 400 °C with a partial oxygen pressure of 7.6 $x10^{-2}$ Torr. Figure 3.1 exhibits two peaks in addition to the sapphire (0001) peaks for indium content x = 1. These diffraction peaks correspond to the (222) and (444) planes of cubic In_2O_3 at 30.34 ° and 63.25 ° respectively. This is in agreement with other single crystal films grown by MBE, MOCVD, and PLD [32], [35], [36]. When the indium content is decreased to x = 0.8 and x = 0.6, the peaks corresponding to (222) and (444) shift to a higher angle. This is due to the smaller ionic radius of Ga^{3+} (0.62 Å) compared to In^{3+} (0.81 Å) and as a result, when gallium replaces indium in the lattice, the lattice constant in the alloy decreases [37]. Figure 3.1(b) is a rocking curve showing the (222) plane for the cubic structures of Indium compositions of x = 1.0, 0.8, and 0.6. These spectra show an increased full width at half maximum (FWHM) corresponding to a decrease in indium content, indicating a decrease in crystal quality. This is probably due to the growth temperature (while optimized for In_2O_3) which probably needs to be higher when gallium is added to the alloy. Since the growth of high quality Ga_2O_3 is carried out at temperature around 550 °C, it is possible that a temperature >400°C would enhance the crystal quality of the $InGaO_3$ alloy.

XRD 2θ-ω scans were taken for indium compositions of x = 0.8 and x = 0.6 as a function of partial oxygen pressure with figure 3.2 representing the XRD spectra for the indium sample with a composition of x = 0.8. The films were grown using flow rates

(top to bottom) of 900, 750, 600, 450, 300, and 0 sccm, which are translated to chamber pressures in figure 3.2(a). For oxygen flow rates ≥ 300 sccm, the single crystal cubic phase is present. Even though the target is stoichiometric, the absence of an oxygen atmosphere during growth results in an amorphous film. Figure 3.2(b) shows the rocking curve around the (222) plane for the x = 0.8 films grown at the oxygen flow rates mentioned above. Based on the XRD spectra, a flow rate of 600 sccm appears to be ideal oxygen level for high crystalline quality films due to the smaller FWHM. This spectra also shows a shift in the (222) peak position for the oxygen flow rates ≥ 600 sccm. While this suggest a change in lattice parameter it is presently not clear as the reason for this. One possibility is a small amount of phase separation in the film. Resolving the cause of this observation requires further investigation.

Additionally, 2θ-ω XRD scans were taken for indium composition x = 0.6 grown under various oxygen pressures. Figure 3.3 displays this XRD spectra which indicates peaks for the cubic (222) and (444) planes for all films grown with an oxygen flow rate ≥ 300 sccm. Two of the samples (flow rate = 450 and 600 sccm) show small additional peaks, which could correspond to the (411) and (400) phase respectively of cubic indium oxide. This was also observed by Gupta *et al.* for the growth of In_2O_3 at different temperatures (400 and 600 °C) and lower pressures (~3.75 $x10^{-4}$ Torr) [34].

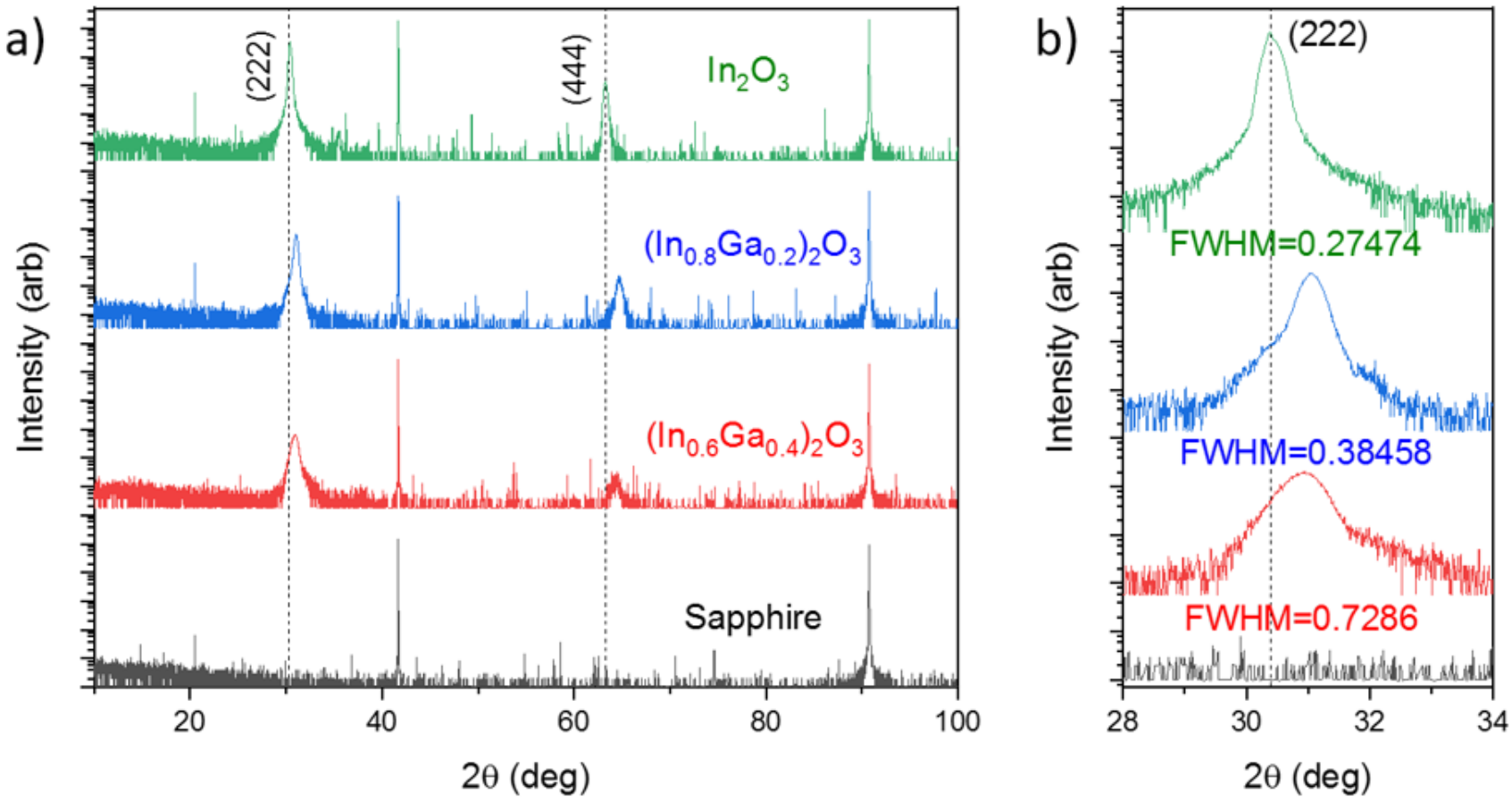

Figure 3.1: XRD 2θ-ω scans (a) and rocking curve (b) of $(InGa)_2O_3$.

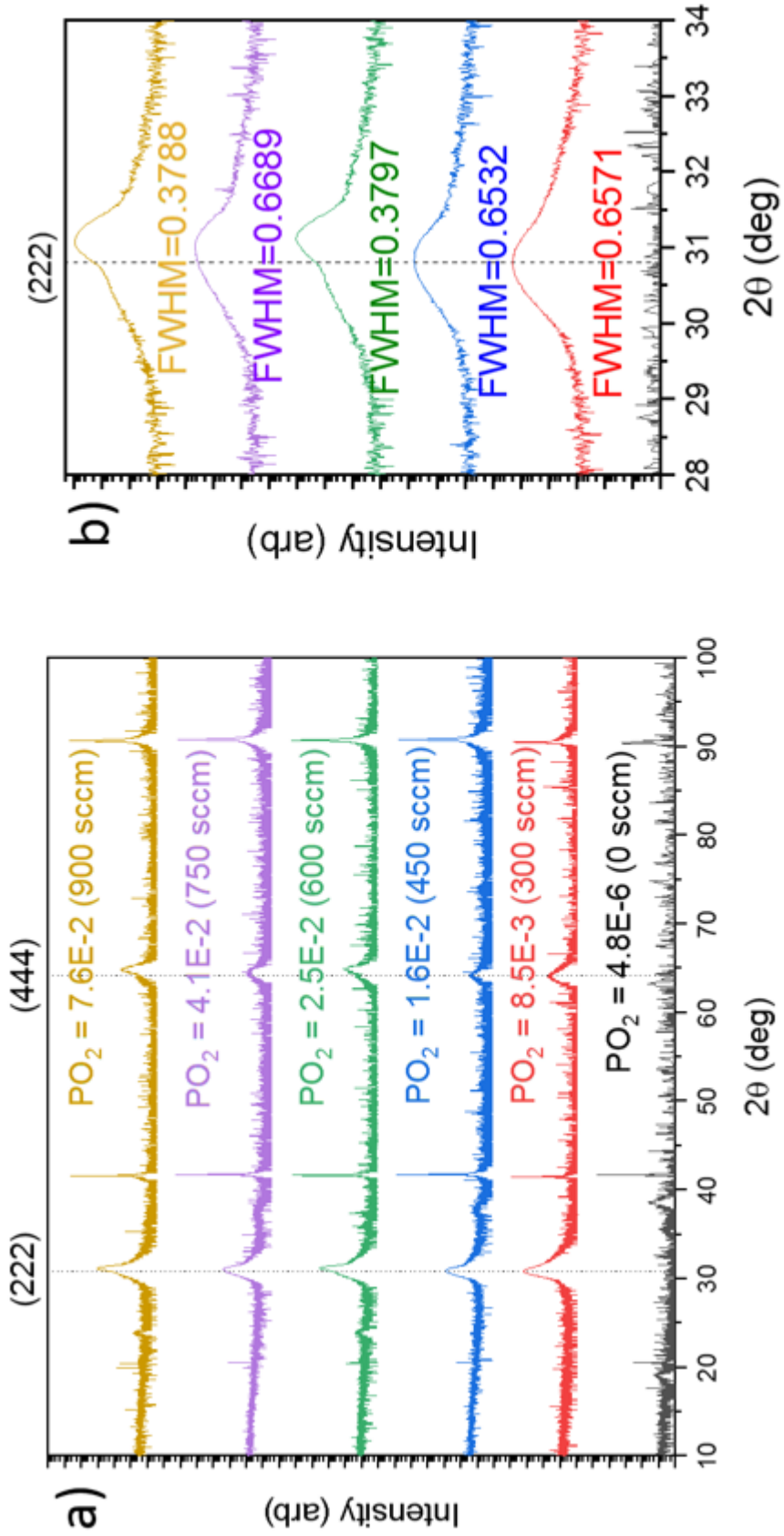

Figure 3.2: XRD 2θ-ω scans (a) and rocking curve (b) of $(In_{0.8}Ga_{0.2})_2O_3$ grown at different oxygen partial pressures.

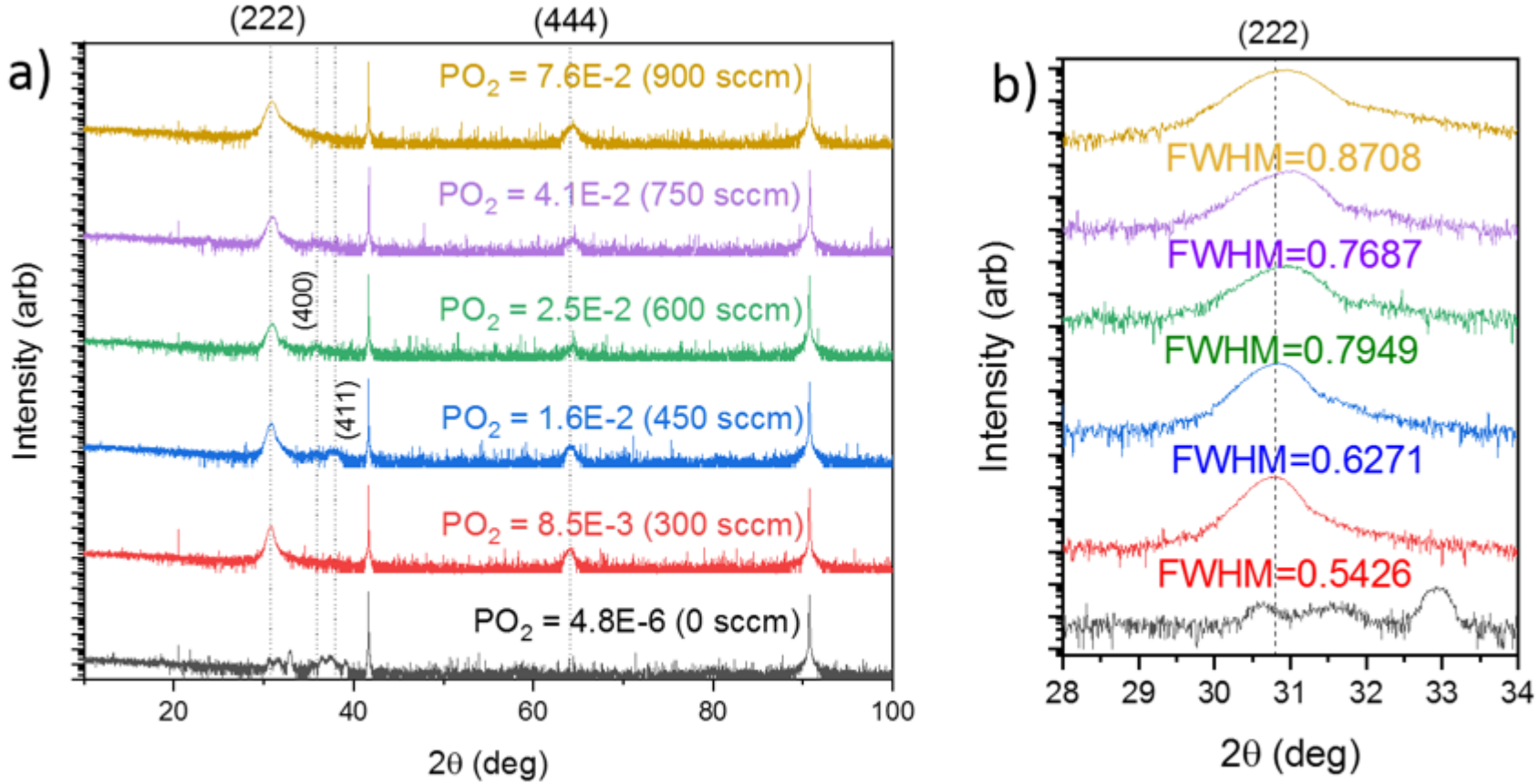

Figure 3.3: XRD 2θ-ω scans (a) and rocking curve (b) of $(In_{0.6}Ga_{0.4})_2O_3$ grown at different oxygen partial pressures.

The chemical composition of the films was analyzed using x-ray photoelectron spectroscopy. Figure 3.4 shows the XPS survey scan of an $(InGa)_2O_3$ alloy with an indium composition of x = 0.6 grown with an oxygen flow rate of 900 sccm. This scan includes the oxygen peak, indium peaks, gallium peaks, a carbon peak, and a nitrogen peak. The carbon peak is present due to the transfer of the sample in air from the PLD to the XPS chamber. The cause of the nitrogen peak is unknown and requires further investigation. No corrections were made to the peak position due to charging effects of the sample. The indium 3d region is analyzed to determine the oxidation state of indium and is shown in Figure 3.5 with the indium $3d_{3/2}$ and indium $3d_{5/2}$ with the indium $3d_{3/2}$ at the higher binding energy.

The deconvolution of the XPS spectrum was done using a Gaussian function on a Shirley background and is shown in figure 3.5 (a), (b), and (c) for oxygen flow rates of 900, 600, and 300 sccm respectively. Complete oxidation of indium is observed at oxygen flow rates of 900 and 600 sccm due to a single peak fit of the experimental data. Evidence of incomplete oxidation for 300 sccm represented by the need for an additional peak for fitting the experimental spectrum. Figure 3.6 shows the O 1s peak at flow rates of 900, 600, and 300 sccm. The peak is fitted with 3 peaks representing oxygen bonded to indium, gallium, and hydroxide from lowest to highest binding energy. The FWHM of the peaks are smallest for the sample grown at 600 sccm. At high oxygen (900 sccm) there may be an excess of O_2, while the growth at low oxygen (300 sccm) an additional peak appears at lower binding energy suggesting incomplete oxidation of the cations.

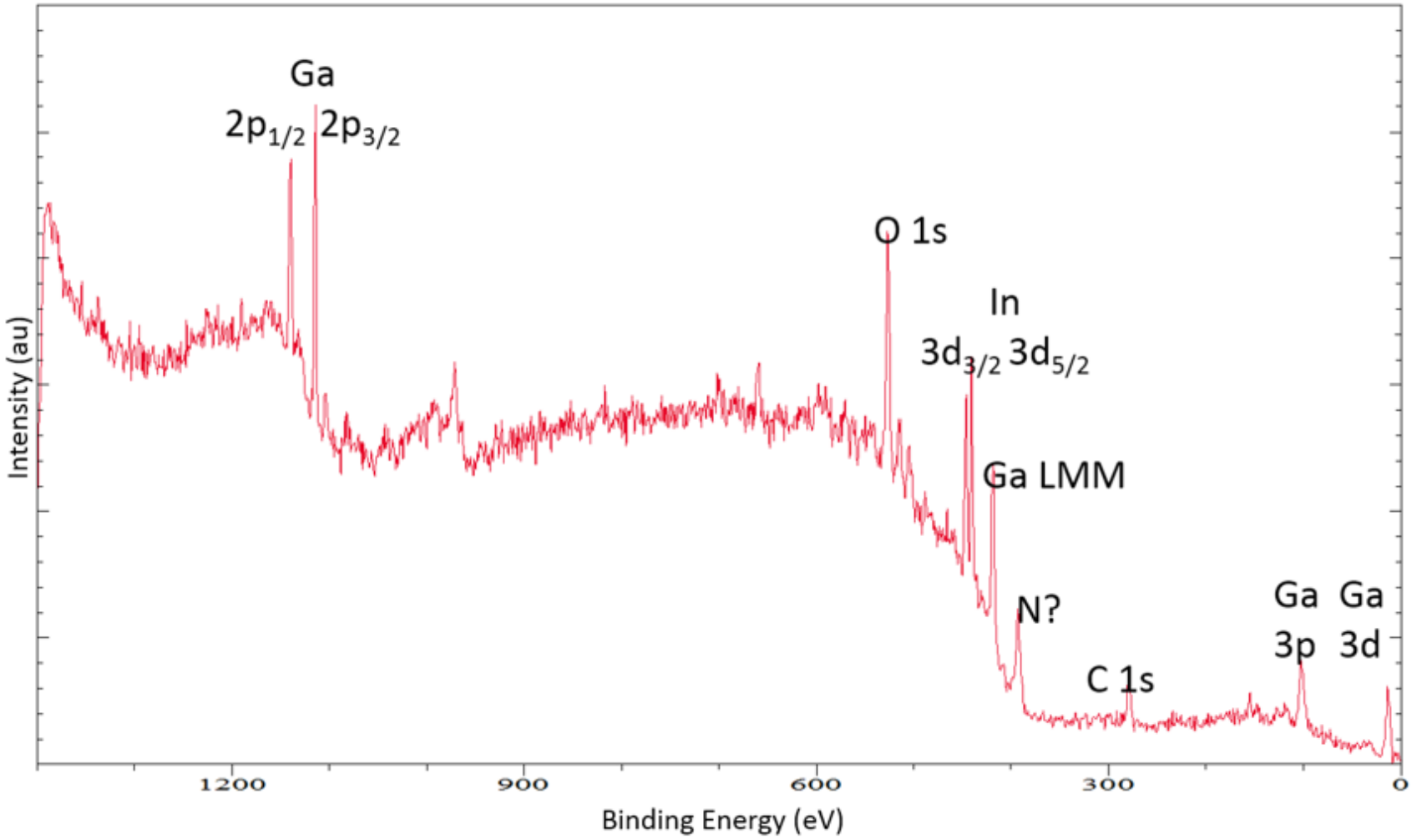

Figure 3.4: XPS survey scan of $(In_{0.6}Ga_{0.4})_2O_3$ film grown with an oxygen flow rate of 900 sccm.

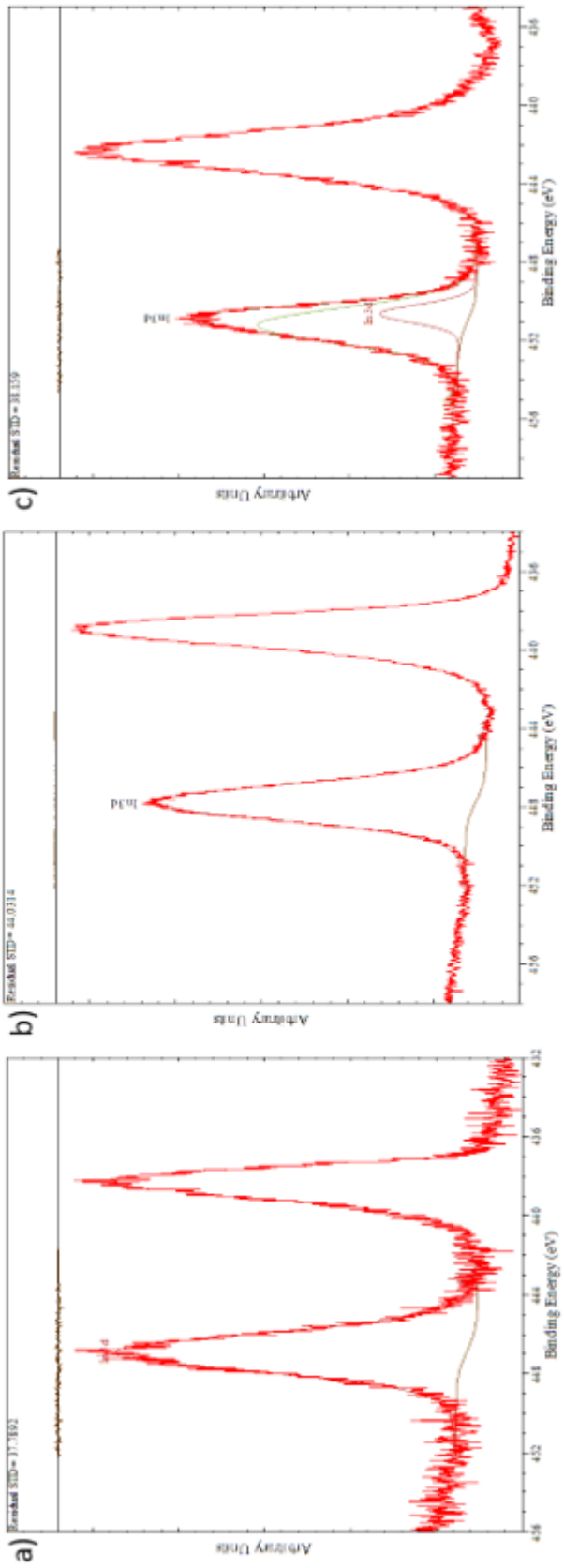

Figure 3.5: XPS of indium 3d core level spectra of 60 % indium composition alloy with an oxygen flow of (a) 900, (b) 600, and (c) 300 sccm.

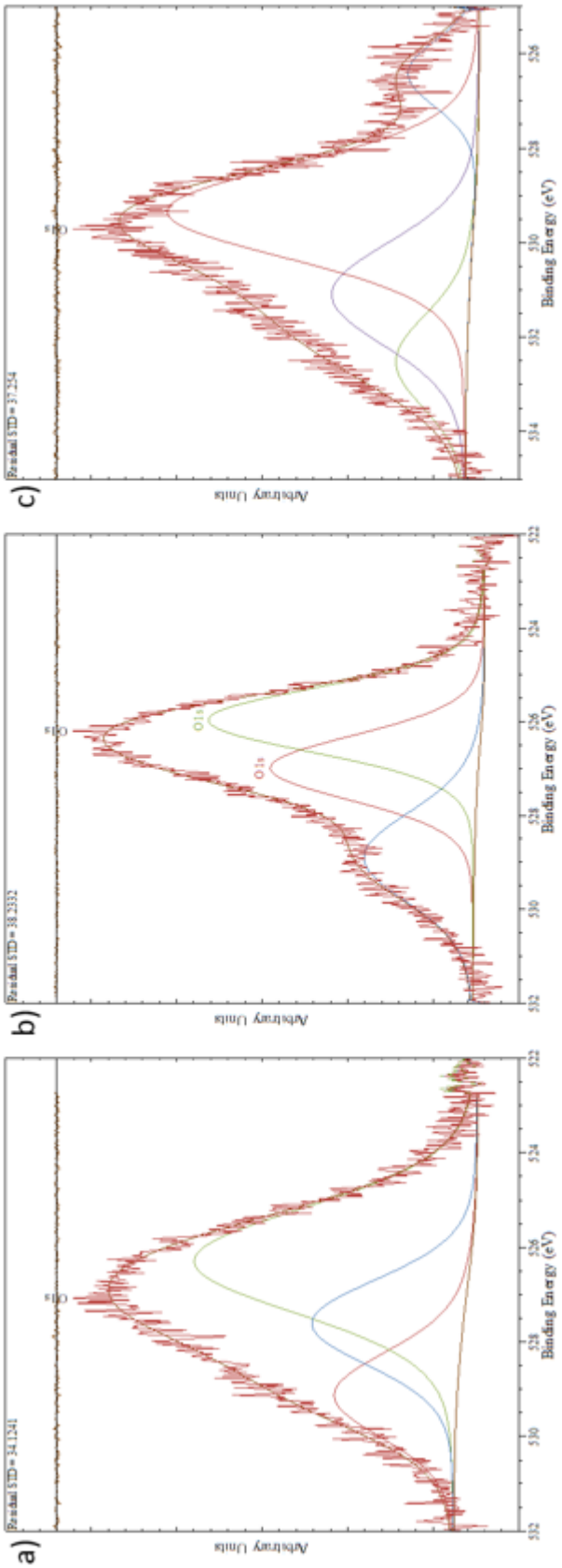

Figure 3.6: XPS of O 1s core level spectra of 60 % indium composition alloy with an oxygen flow of (a) 900, (b) 600, and (c) 300 sccm.

Spectroscopic ellipsometry measurements were taken to investigate the effect of oxygen partial pressure on the optical properties of these films. Figure 3.7(a) displays the psi and delta values obtained from the measurement on an 80 % indium composition sample grown using an oxygen flow rate of 900 sccm along with the Cauchy model used to fit the data. The refraction index (n) and extinction coefficient (k) extracted from the model and displayed as a function of wavelength in Figure 3.7(b). The n and k values for all of the grown alloys are shown as a function of oxygen pressure and flow rate in Figure 3.8(a). The refraction index for the 80 % indium composition sample reduces from 2.00 to 1.88 with the increased oxygen flow from 300 to 750 sccm respectively. At an oxygen flow rate of 900 sccm, the refractive index shows an increase to a value of n = 2.05. A similar trend appears for the samples containing 60 % indium. The refraction index decreases from 2.06 to 1.88 with an increased flow from 300 to 600 sccm. The samples with oxygen flow rates between 600 and 900 sccm are virtually unchanged at a value of n = 1.88.

In addition, film thickness and roughness are extracted from the modeled ellipsometry data and displayed in Figure 3.8(b). The alloys containing 80 % indium show a thickness of ~90 nm when grown at an oxygen flow rate of 300 and 450 sccm. At

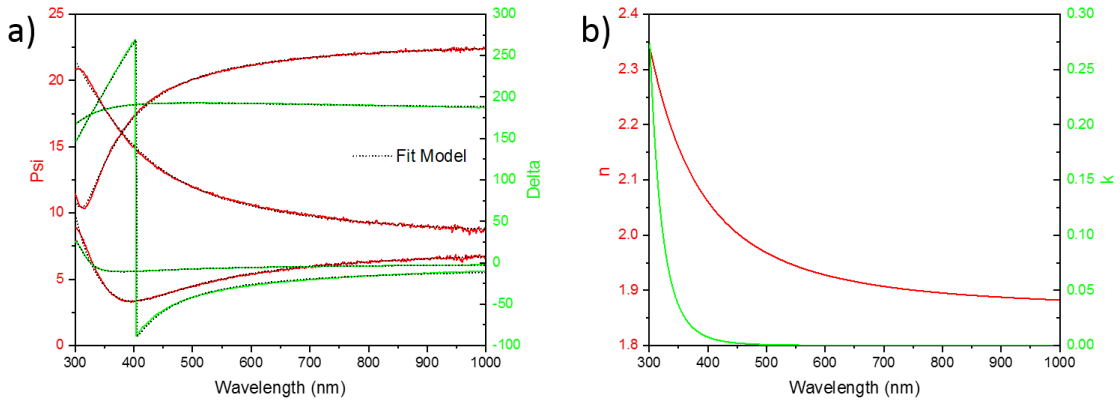

Figure 3.7: Ellipsometry graph of (a) psi, delta, and the fit model as a function of wavelength and (b) the optical constants (n, k) for $(In_{0.8}Ga_{0.2})_2O_3$ grown with an oxygen flow rate of 900 sccm.

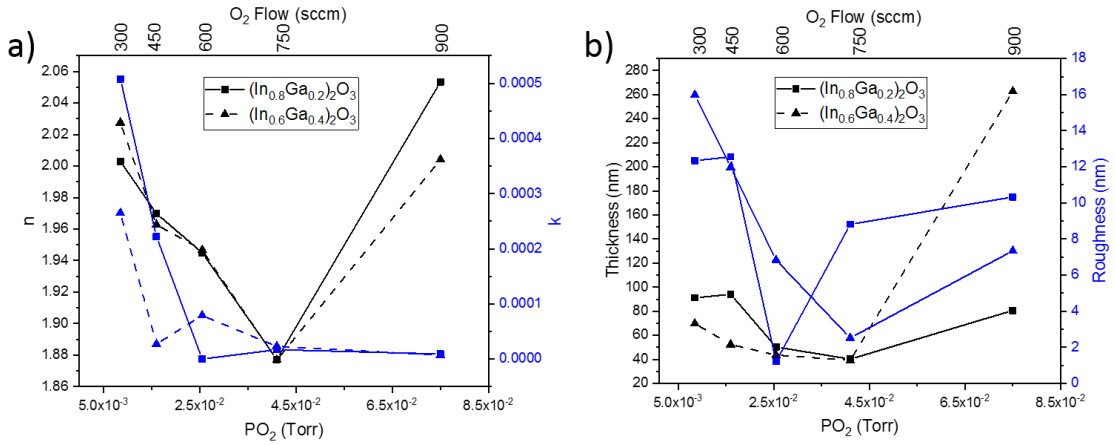

Figure 3.8: Optical constants n and k (a) and thickness and roughness (b) for $(InGa)_2O_3$ alloys as a function of oxygen partial pressure.

600 and 700 sccm, the thickness of the films reduce to 50 and 40 nm respectively before thickness increases to 80 nm at a flow rate of 900 sccm. Roughness of these alloys shows a decrease from about 12 nm for the 300 and 450 sccm oxygen flow rate down to 1.6 nm for the sample grown at 600 sccm. The roughness again increases to 9 and 10 nm for the 750 and 900 sccm films. The 60 % indium composition alloys show a similar trend to the film thickness as the 80 % indium compositions. With an increase of oxygen flow from 300 to 750 sccm, the thickness of the films reduce from 70 to 40 nm. The thickness generated from the model for the alloy grown at an oxygen flow rate of 900 sccm is ~260 nm. This is an unexpected deviation from previous samples and is attributed to a possible modeling error which needs further investigation. Roughness of these samples show a decrease from 16 nm at a flow rate of 300 sccm down to 3 nm with the increase in oxygen to 750 sccm. The roughness increases to 7.5 nm for the sample grown with a flow rate of 900 sccm.

Further investigation into the optical properties of these alloys was carried out by taking UV-Vis transmittance measurements of the films using an oxygen flow rate of 900 sccm. The three alloys with indium compositions of x = 1.0, 0.8, and 0.6 all showed

transmittance greater than 90 % indium the visible wavelengths and are displayed in figure 3.9 (a). These values are in agreement with the transmission values found by Oshima and Fujita [17]. Figure 3.9(b) shows the Tauc plot generated using the transmittance measurements. A Tauc plot provides a method for determining the band gap using the absorbance data plotted with respect to photon energy. It shows the bandgap for the 100 % indium composition sample to be 3.68 eV and increases with an increased gallium composition. This increased bandgap with an increase of gallium is in agreement with the results found by von Wenckstern *et al.* [53].

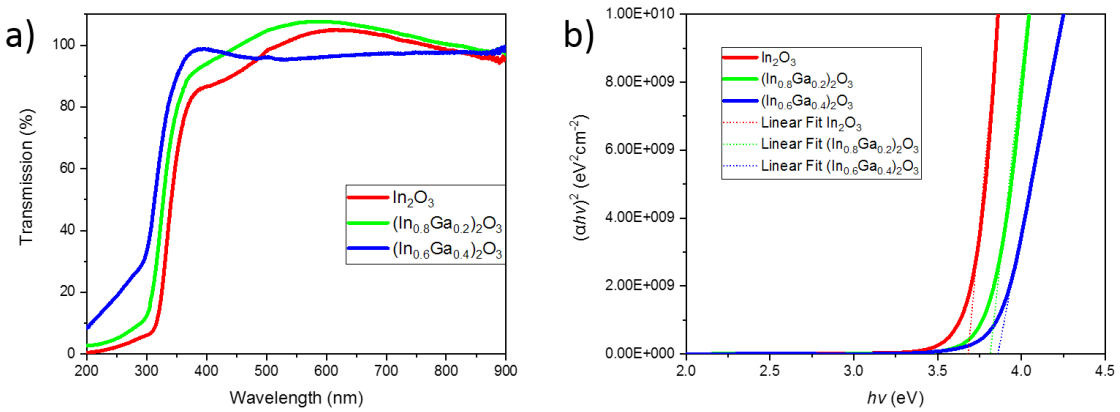

Figure 3.9: Transmittance spectra (a) and Tauc plot showing the bandgap (b) for $(In_{0.8}Ga_{0.2})_2O_3$ grown with an oxygen flow rate of 900 sccm.

3.2 Heterostructure Fabrication

3.2.1 Experimental

Additionally, $In_2O_3/(InGa)_2O_3$ heterostructures are fabricated on sapphire (0001) substrates using the same parameters discussed above with the exception of the oxygen partial pressure. The oxygen flow rate during growth for these films is fixed at 900 sccm while the prior structures had rates of 300, 450, 600, 750, and 900 sccm. Each layer is grown for 30 minutes (18000 laser pulses) at a substrate temperature of 400 °C. A diagram of the film structure is shown in figure 3.10.

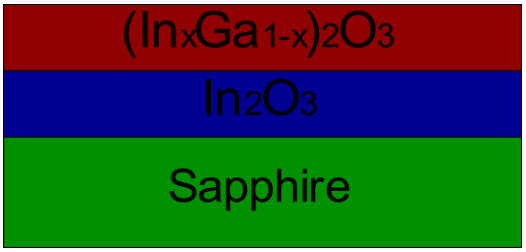

Figure 3.10: Diagram of the $In_2O_3/(In_xGa_{1-x})_2O_3$ heterostructure.

3.2.2 Results and Discussion

XRD diffraction is used to determine the crystalline properties of these layered films. The two theta-omega (2θ-ω) XRD scans of the $In_2O_3/(In_xGa_{1-x})_2O_3$ thin films grown on sapphire are shown in figure 3.11 for indium contents x = 0.8 and 0.6. These XRD spectra indicate the formation of a heterostructure between the In_2O_3-$(In_xGa_{1-x})_2O_3$ thin films. The structure containing the 80 % indium composition film on In_2O_3 shows each layer clearly with the left peak of the (222) orientation belonging to In_2O_3 and the right peak belonging to the alloy. This shift is more pronounced along the (444) orientation. This separation is less pronounced in the heterostructure containing the 60 % indium content. This is due to the reduced peak shift of the 60 % indium composition in comparison to the peak shift of the 80 % indium composition sample. This peak shift was shown earlier in figures 3.2(b) and 3.3(b) at an oxygen flow rate of 900 sccm. This opens up the possibility of fabricating HEMT structures where a 2-dimensional electron gas (2DEG) can appear at the heterointerface. This can also be used to design quantum well structures to tune the bandgap. Additionally, these heterostructures could be suitable for use in UV optoelectronics.

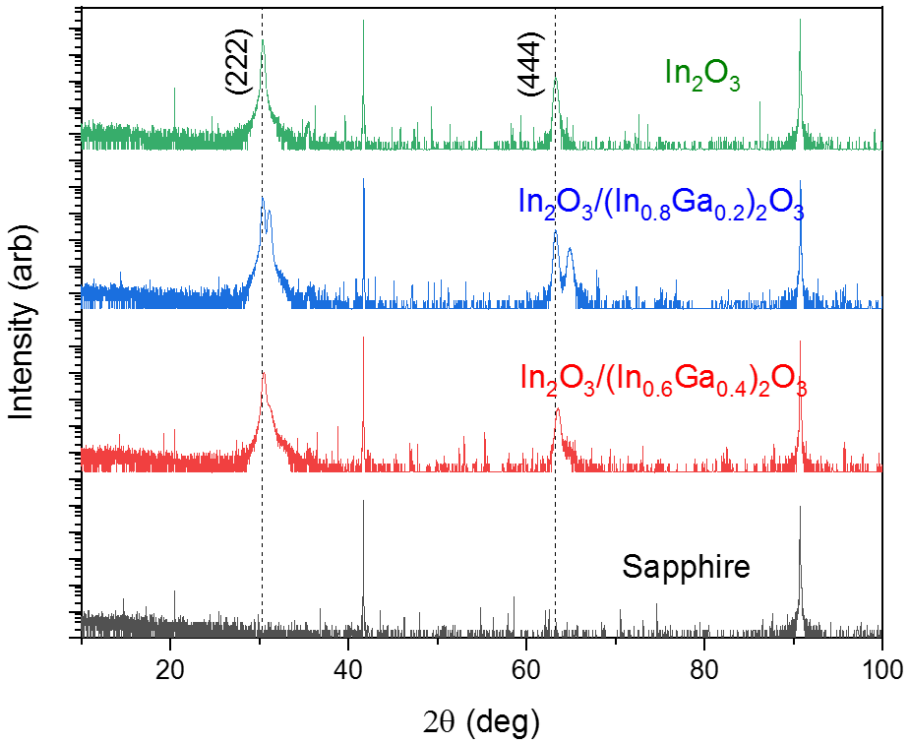

Figure 3.11: XRD 2θ-ω scans of $In_2O_3/(InGa)_2O_3$ heterostructures.

IV. CONTACT FABRICATION AND ELECTRICAL CHARACTERIZATION

4.1 Experimental

To deposit the metal contacts, a photolithographic process was used to pattern the features. The process flow is indicated in figure 4.1. Prior to application of the photoresist, the wafer was cleaned with organic solvents (acetone, methanol, and isopropanol). A negative lift-off resist (KL 1607) was applied using a spin coater at 3000 rpm for 45 seconds. A soft-bake was performed on a contact hotplate at 115 °C for 60 seconds. The SUSS Microtech MJB4 contact mask aligner was used to expose the resist with an intensity of 50.1 mW/cm^2 at a wavelength of 405 nm for 7 seconds. A post-exposure bake was performed on the hotplate at 115 °C for 60 seconds. The developer was applied at a speed of 5 rpm for 5 seconds, then a stationary developing time of 40 seconds and finally rinsed with deionized water. The pattern was then inspected for quality under magnification prior to metal deposition. A portion of the photomask used is shown in figure 4.2. This mask includes parallel bars for the transmission line measurements (TLM) at spacings of 100, 200, 300, 400, and 500 µm with a length of 100

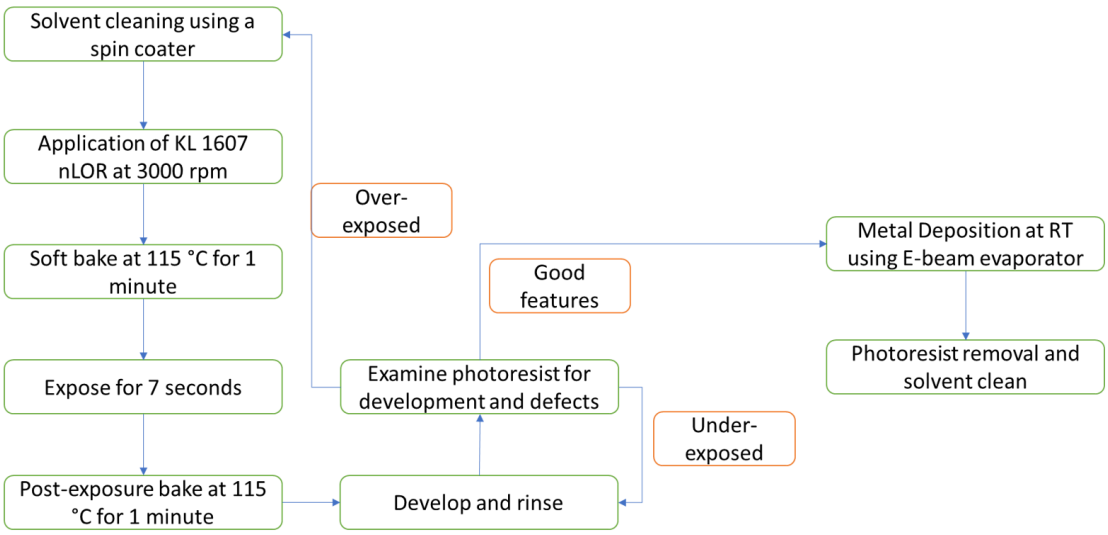

Figure 4.1: Fabrication process for metal deposition.

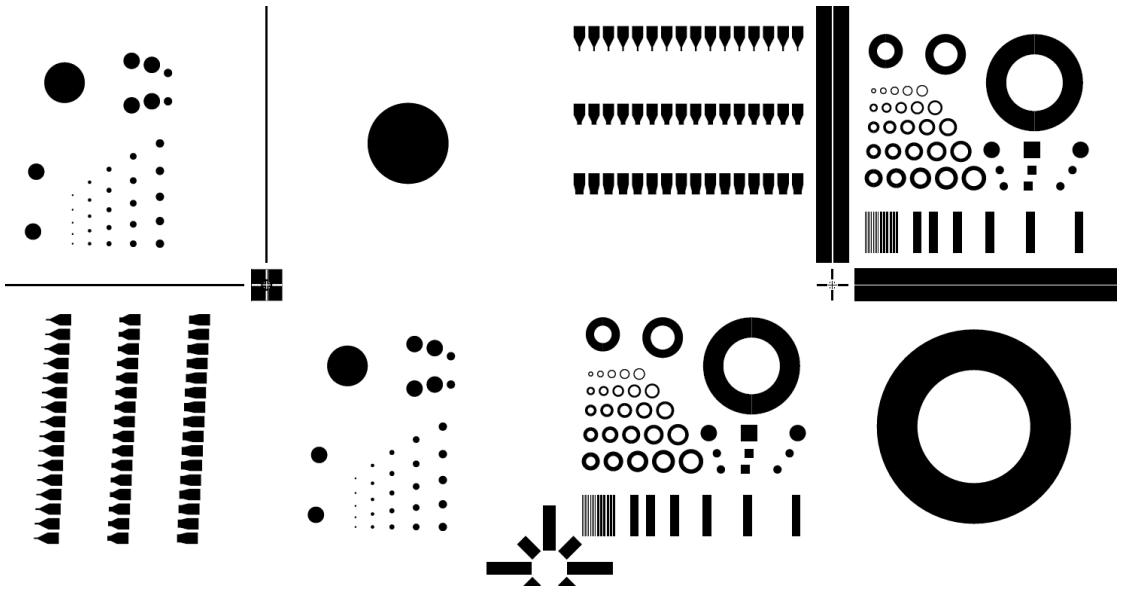

Figure 4.2: Partial diagram of the photomask used for the deposition of metal contacts.

μm and width of 500 μm, and contact structures for linear and ring diodes at various sizes. Current-Voltage (I-V) measurements were taken across each spacing using a Keysight B1500A semiconductor device analyzer.

The metal deposition was performed using the Angstrom EvoVac electron-beam evaporator. The metals deposited on the films include Ni, Cu, and Ir at a thickness of 100 nm each and metal stacks of Ti/Al and Ti/Au at a thickness of 50/100 nm. The metals were deposited at room temperature at a rate of 0.5 Å/s for the initial 100 Å and increased to 1.0 Å/s for the remainder of the deposition. The lift-off resist is then removed by ultrasonication in acetone for 15 minutes and cleaned with methanol and isopropanol and dried with nitrogen gas.

In addition to these measurements, a BioRad Hall measurement unit was used to determine the electrical characteristics of the films. Metallic indium is soldered onto the corners of ~1 cm x 1 cm square samples to create the contacts and alloy at 450 °C in a N_2

ambient for 15 minutes to produce ohmic contacts. These measurements are taken to determine the resistivity, carrier concentration, and mobility of the films.

4.2 Results and Discussion

Current-Voltage measurements were taken across each spacing of the TLM structure for each metal. Figure 4.3 displays the I-V curves for metals deposited on a film with an indium composition of 80 % grown at an oxygen flow rate of 600 sccm. The dashed line in figure 4.2 represents the I-V curve for a sample doped with 1 % silicon by weight under the same conditions. Each of the metal contact structures show a linear current-voltage relationship, indicating ohmic contacts. Although Schottky

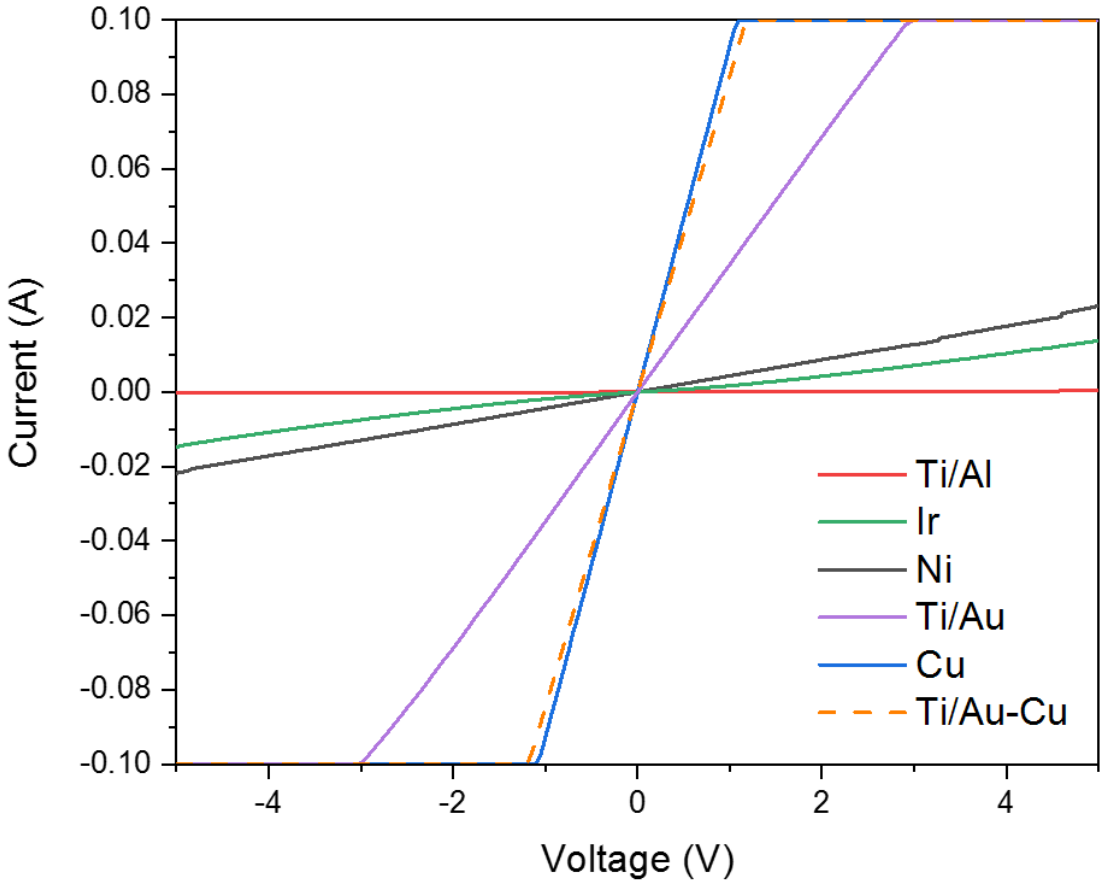

Figure 4.3: Current-voltage measurements of various metal contacts (dashed sample is doped with 1 % Si by weight).

contacts have not been reported to date for undoped indium oxide, they have been reported for Si-doped gallium oxide using copper as the Schottky contact [54]. Note that the horizontal portions of the I-V curves located at +/- 0.1 amp are due to the current threshold set in the semiconductor device analyzer.

The I-V measurements taken from the TLM structure were converted to resistance and plotted as a function of distance between the contacts and are shown in figure 4.4. It should be noted that the results from these measurements are not believed to be accurate due to a majority of the calculated transfer lengths were in excess of double the contact length. It was later found that the accuracy of the measurements are dependent on the geometry of the TLM structure and the resistivity of the film as demonstrated in a thesis

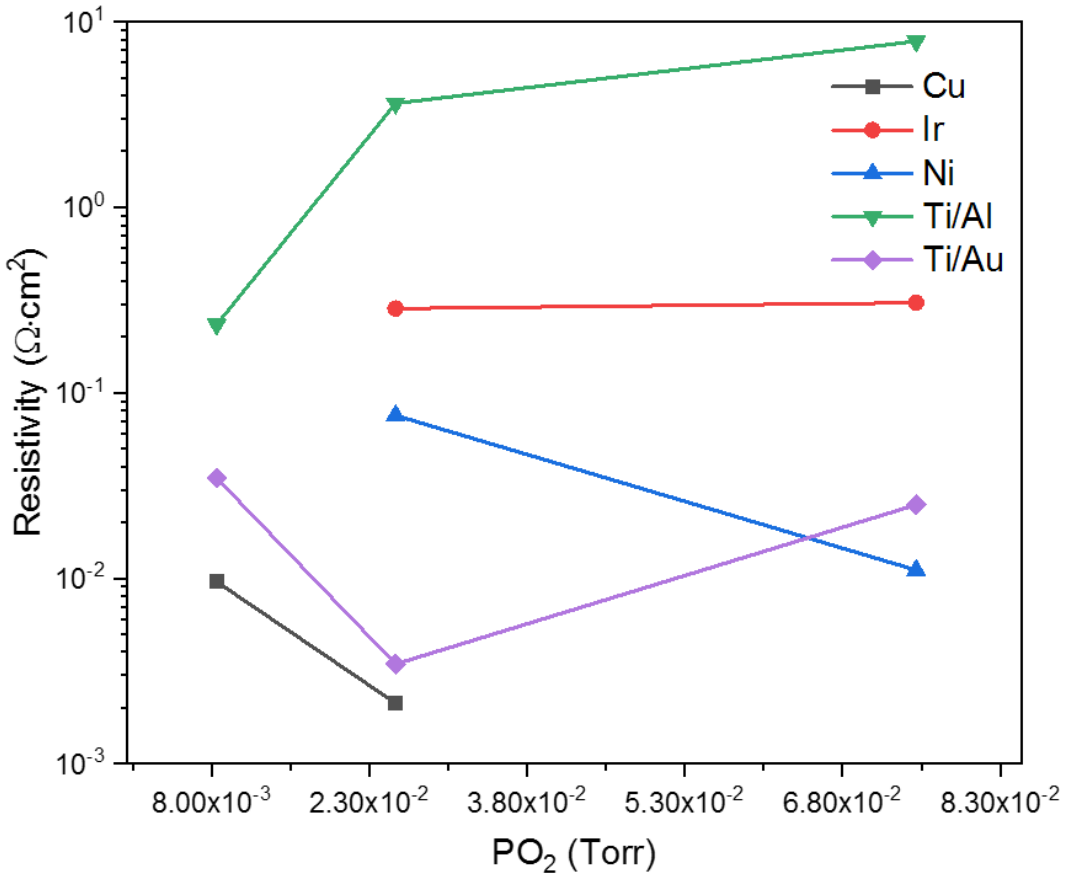

Figure 4.4: Resistivity of 80 % In composition $(InGa)_2O_3$ alloys at various pressures determined by transmission line measurements.

by Sidhant Grover [52]. According to Grover's work, the TLM structure geometry should have been designed with smaller contact lengths with a reduced spacing.

The Hall measurements were taken for indium compositions of 80 and 60 % at various pressures and are shown in figures 4.5 and 4.6 respectively. Figure 4.5(a) shows the 80 % Indium sample over a range of oxygen pressures. The resistivity increases from ~5.0 x10^{-4} to 2.0 x10^{-2} Ω·cm with an increase in oxygen partial pressure from 8.5 x10^{-3} to 4.1 x 10^{-2} torr, then decreases to 4.0 x10^{-3} Ω·cm at a partial pressure of 7.6 x10^{-2} torr. Measurements for the sample doped with 1 % Si by weight were only taken for oxygen flow rates of 300, 600, and 900 sccm, but the sample at 900 sccm is not shown due to the high resistance of the metal indium contacts. These sample show a decrease in resistance from 2.6 x10^{-3} to 1.0 x10^{-3} Ω·cm with an increase in the flow rate from 300 to 600 sccm. The Hall mobility for the undoped samples show a decrease in mobility from 49.9 to 15.2 $cm^2/(V·s)$ for the flow rates of 300 and 600 sccm respectively. The carrier concentration for these samples is shown with Hall mobility as a function of oxygen partial pressure in figure 4.5(b). The samples grown at the lowest oxygen partial pressures (8.5 x10^{-3} and 1.6 x10^{-2} torr) possess the greatest carrier concentration of 1.2 x10^{20} and 1.3 x10^{20} cm^{-3}

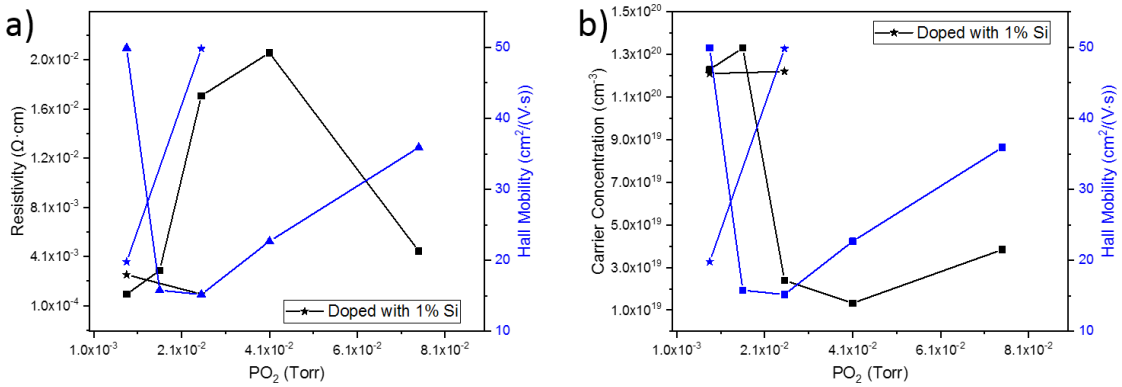

Figure 4.5: Hall measurements for 80 % In composition alloys displaying (a) resistivity and Hall mobility and (b) carrier concentration and Hall mobility as a function of oxygen partial pressure.

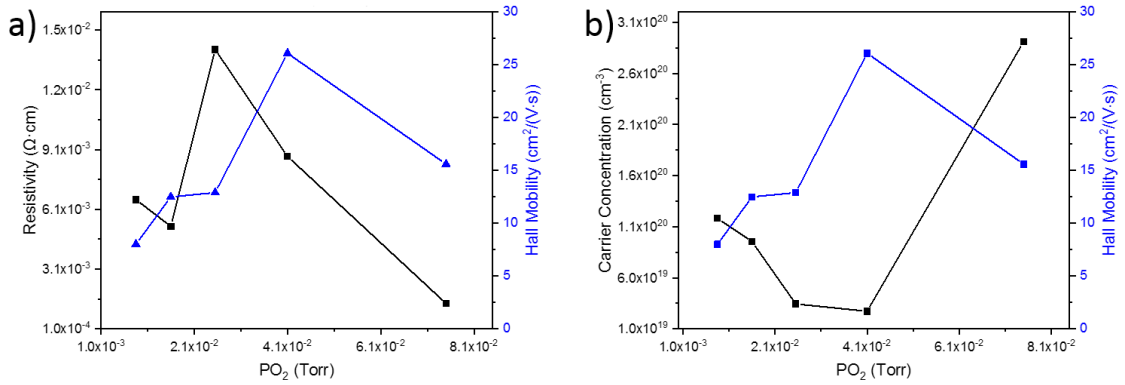

Figure 4.6: Hall measurements for 60 % In composition alloys displaying (a) resistivity and Hall mobility and (b) carrier concentration and Hall mobility as a function of oxygen partial pressure.

respectively. For pressures ≥ 2.55 x10^{-3} torr, the carrier concentration reduces by a factor of 10. The carrier concentration for the sample doped with 1 % silicon are similar to the undoped sample at 8.5 x10^{-3} torr with a value of 1.2 x10^{20} cm^{-3}, but at 2.55 x10^{-3} torr the carrier concentration for the doped sample are greater than the undoped sample by a factor of 10. The increase in carrier concentration for the films grown at lower oxygen partial pressure can be attributable to an increase in the oxygen vacancies consistent with the XPS data.

The Hall data collected from the 60 % indium composition sample (figure 4.6(a)) shows a maximum resistivity of 1.4 x10^{-2} Ω·cm at a partial pressure of 2.55 x10^{-2} torr and a minimum resistivity of 1.4 x10^{-3} Ω·cm at a pressure of 7.5 x10^{-2} torr. The Hall mobility increases from 8.0 $cm^2/(V·s)$ to a maximum of 26.1 $cm^2/(V·s)$ for an increasing pressure from 8.5 x10^{-3} to 4.1 x10^{-2} torr. Figure 4.6(b) displays the carrier concentration for the samples with a 60 % indium composition. The maximum concentration found is 2.9 x10^{20} cm^{-3} at a pressure of 7.5 x10^{-2} torr while the remaining samples increase concentration with a decrease in pressure.

Overall, the resistivity of the samples with an 80 % indium composition are higher than the samples composed of 60 % indium. There appears to be little difference

in carrier concentration between the two samples, but the Hall mobility does show lower values in the 60 % sample.

V. CONCLUSION AND FUTURE WORK

5.1 Conclusion

The objective of this research is study the growth and characterization of wide bandgap semiconductor $(In_xGa_{1-x})_2O_3$ thin films for $x \geq 0.6$. These represent potential candidates for applications including UV optoelectronics, high-power devices, and heterostructures for use in HEMTs. Another part of this research is to investigate the properties of various metals deposited on the oxide layers. A process was demonstrated for the fabrication of single crystal cubic In_2O_3 films and its alloys with gallium. X-ray diffraction measurements show an increase in the lattice parameter with increase in indium content of the films as expected due to the larger size of indium atoms. The optical properties of the films (refractive indices and extinction coefficients) were extracted from spectroscopic ellipsometry. The optical bandgap was determined using UV-Vis measurements and the optical bandgap measured for In_2O_3 agrees with values reported in literature. The bandgap was found to increase with an increase in gallium content. XPS measurements suggest an optimized partial oxygen pressure during growth for complete oxidation of the cations. Hall measurements were used to determine the resistivity, carrier concentration, and Hall mobility of the $(InGa)_2O_3$ alloys. A reduction of the mobility was found with an increase in gallium content in the alloys, while all samples retained a carrier concentration greater than 10^{19} cm^{-3}. A number of metals were deposited by e-beam evaporation and all show ohmic behavior. Lastly, heterostructures comprised of In_2O_3 and $(InGa)_2O_3$ have been fabricated which opens up the possibility for high mobility 2DEG and bandgap engineering in this material.

5.2 Future Work

Further exploration of the growth parameters with various gallium contents is required. As a result of the findings discussed within this research, growth of the $(InGa)_2O_3$ alloys will be investigated using a higher growth temperature with the goal of a higher-quality crystal structure. Further XPS investigations will need to be carried out for a complete study the oxidation states of the cations. Additionally, the electrical and optical properties of the heterostructures will be investigated. The fabrication of optoelectronic devices will be conducted and characterized. Lastly, electronic devices fabricated using heterostructures with Ga_2O_3 will be investigated to demonstrate the potential of this exciting class of material.

REFERENCES

[1] S. Muller *et al.*, "Comparison of Schottky contacts on β-gallium oxide thin films and bulk crystals," *Appl. Phys. Express*, vol. 8, no. 12, p. 121102, Nov. 2015.

[2] L. M. Tolbert, "Power Electronics for Distributed Energy Systems and Transmission and Distribution Applications: Assessing the Technical Needs for Utility Applications," ORNL, ORNL/TM-2005/230, Dec. 2005.

[3] K. O. Armstrong, S. Das, and J. Cresko, "Wide Bandgap Semiconductor Opportunities in Power Electronics," in *2016 IEEE 4th Workshop on Wide Bandgap Power Devices and Applications (WiPDA)*, Fayetteville, AR, USA, 2016, pp. 259–264.

[4] X. She, A. Q. Huang, O. Lucia, and B. Ozpineci, "Review of Silicon Carbide Power Devices and Their Applications," *IEEE Trans. Ind. Electron.*, vol. 64, no. 10, pp. 8193–8205, Oct. 2017.

[5] M. Higashiwaki, A. Kuramata, H. Murakami, and Y. Kumagai, "State-of-the-art technologies of gallium oxide power devices," *J. Phys. Appl. Phys.*, vol. 50, no. 33, p. 333002, 2017.

[6] E. F. Schubert, *Light-Emitting Diodes*. Cambridge University Press, 2003.

[7] I. Akasaki, H. Amano, and S. Nakamura, "Efficient Blue Light-emitting Diodes Leading to Bright and Energy-saving White Light Sources," *AAPPS Bull.*, vol. 24, no. 6, p. 3, Dec. 2014.

[8] L. X. Qian, Y. Wang, Z. H. Wu, T. Sheng, and X. Z. Liu, "β-Ga_2O_3 solar-blind deep-ultraviolet photodetector based on annealed sapphire substrate," *Vacuum*, vol. 140, no. Supplement C, pp. 106–110, Jun. 2017.

[9] S. Shanmugan, D. Mutharasu, and I. Kamarulazizi, "Rhombohedral In_2O_3 thin films preparation from in metal film using Oxygen plasma," in *2012 10th IEEE International Conference on Semiconductor Electronics (ICSE)*, 2012, pp. 711–715.

[10] M. F. Bekheet *et al.*, "Orthorhombic In_2O_3: A Metastable Polymorph of Indium Sesquioxide," *Angew. Chem. Int. Ed.*, vol. 52, no. 25, pp. 6531–6535.

[11] T. de Boer, A. Moewes, M. F. Bekheet, A. Gurlo, and R. Riedel, "Band gap and electronic structure of cubic, rhombohedral, and orthorhombic In_2O_3 polymorphs: Experiment and theory," *Phys. Rev. B*, vol. 93, no. 15, Apr. 2016.

[12] S. Z. Karazhanov, P. Ravindran, P. Vajeeston, A. Ulyashin, T. G. Finstad, and H. Fjellvåg, "Phase stability, electronic structure, and optical properties of indium oxide polytypes," *Phys. Rev. B*, vol. 76, no. 7, p. 075129, Aug. 2007.

[13] G. Giusti, "Deposition and characterisation of functional ITO thin films," Ph.D., University of Birmingham (United Kingdom), England, 2011.

[14] S. I. Stepanov, V. I. Nikolaev, V. E. Bougrov, and A. E. Romanov, "Gallium oxide: Properties and applications - A review," *Rev. Adv. Mater. Sci.*, vol. 44, no. 1, pp. 63–86, 2016.

[15] Y. Yao *et al.*, "Growth and characterization of α-, β-, and ϵ-phases of Ga_2O_3 using MOCVD and HVPE techniques," *Mater. Res. Lett.*, vol. 6, no. 5, pp. 268–275, 04 2018.

[16] S.-D. Lee, Y. Ito, K. Kaneko, and S. Fujita, "Enhanced thermal stability of alpha gallium oxide films supported by aluminum doping," *Jpn. J. Appl. Phys.*, vol. 54, no. 3, p. 030301, Feb. 2015.

[17] T. Oshima and S. Fujita, “Properties of Ga2O3-based $(In_xGa_{1-x})_2O_3$ alloy thin films grown by molecular beam epitaxy,” *Phys. Status Solidi C*, vol. 5, 2008.

[18] M. Bender *et al.*, “Dependence of the photoreduction and oxidation behavior of indium oxide films on substrate temperature and film thickness,” *J. Appl. Phys.*, vol. 90, no. 10, p. 5382, Nov. 2001.

[19] O. Bierwagen, “Indium oxide—a transparent, wide-band gap semiconductor for (opto)electronic applications,” *Semicond. Sci. Technol.*, vol. 30, no. 2, p. 024001, 2015.

[20] Y. Wu, C. H. M. Marée, and R. F. Haglund, “Resistivity and oxygen content of indium tin oxide films deposited at room temperature by pulsed-laser ablation,” *J. Appl. Phys.*, vol. 86, no. 2, pp. 991–994, Jul. 1999.

[21] S. H. Kim, N.-M. Park, T. Kim, and G. Sung, “Electrical and optical characteristics of ITO films by pulsed laser deposition using a 10 wt.% SnO_2-doped In_2O_3 ceramic target,” *Thin Solid Films*, vol. 475, no. 1, pp. 262–266, Mar. 2005.

[22] S. Kaleemulla, A. S. Reddy, S. Uthanna, and P. S. Reddy, “Physical properties of In_2O_3 thin films prepared at various oxygen partial pressures,” *J. Alloys Compd.*, vol. 479, pp. 589–593, Jan. 2009.

[23] F. Xia, X. Zhang, M. Wang, J. Xu, and Q. Liu, “Analysis of the laser oxidation kinetics process of In-In_2O_3 MTMO photomasks by laser direct writing,” *Opt. EXPRESS*, vol. 23, no. 22, pp. 29193–29201, Nov. 2015.

[24] “Indium Oxide,” *American Elements*. [Online]. Available: https://www.americanelements.com/indium-oxide-1312-43-2. [Accessed: 07-Jul-2018].

[25] A. Schleife *et al.*, "Optical properties of In_2O_3 from experiment and first-principles theory: influence of lattice screening," *New J. Phys.*, vol. 20, no. 5, p. 053016, 2018.

[26] M. Girtan, "Investigations on the optical constants of indium oxide thin films prepared by ultrasonic spray pyrolysis," *Mater. Sci. Eng. B*, vol. 118, no. 1, pp. 175–178, Apr. 2005.

[27] P. Guo *et al.*, "Low-Loss Near-Infrared Hyperbolic Metamaterials with Epitaxial ITO-In_2O_3 Multilayers," *ACS Photonics*, vol. 5, no. 5, pp. 2000–2007, May 2018.

[28] R. E. Agbenyeke, E. A. Jung, B. K. Park, T.-M. Chung, C. G. Kim, and J. H. Han, "Thermal atomic layer deposition of In_2O_3 thin films using dimethyl(N-ethoxy-2,2-dimethylcarboxylicpropanamide)indium and H_2O," *Appl. Surf. Sci.*, vol. 419, pp. 758–763, Oct. 2017.

[29] K. Shamsoddini and H. Eshghi, "Effect of Deposition Rate and Annealing on Physical Properties of In_2O_3 Thin Films Prepared by Spray Pyrolysis: Ultraviolet (UV) Photoconductivity Response," *J. Electron. Mater.*, vol. 46, no. 7, pp. 4649–4655, Jul. 2017.

[30] M. Zervos, D. Tsokkou, M. Pervolaraki, and A. Othonos, "Low Temperature Growth of In_2O_3 and InN Nanocrystals on Si(111) via Chemical Vapour Deposition Based on the Sublimation of NH_4Cl in In," *Nanoscale Res. Lett.*, vol. 4, no. 6, pp. 491–497, Jun. 2009.

[31] C. Y. Wang *et al.*, "Phase selective growth and properties of rhombohedral and cubic indium oxide," *Appl. Phys. Lett.*, vol. 89, no. 1, p. 011904, Jul. 2006.

[32] C. Zhao, Z. Li, W. Mi, C. Luan, X. Feng, and J. Ma, "Structure and Optical Properties of Epitaxial Indium Oxide Films Deposited on Y-Stabilized ZrO_2 (111) by MOCVD," *J. Electron. Mater.*, vol. 44, no. 8, pp. 2719–2724, Aug. 2015.

[33] N. Taga, M. Maekawa, Y. Shigesato, I. Yasui, M. Kamei, and T. E. Haynes, "Deposition of Heteroepitaxial In_2O_3 Thin Films by Molecular Beam Epitaxy," *Jpn. J. Appl. Phys.*, vol. 37, no. 12R, p. 6524, Dec. 1998.

[34] R. K. Gupta, N. Mamidi, K. Ghosh, S. R. Mishra, and P. K. Kahol, "Growth and characterization of In_2O_3 thin films prepared by pulsed laser deposition," *J. Optoelectron. Adv. Mater.*, vol. 9, no. 7, pp. 2211–2216, Jul. 2007.

[35] J. Stankiewicz, X. Torrelles, J. L. García-Muñoz, and J. Blasco, "Structural and electrical properties of indium oxide thin films grown by pulsed laser deposition in oxygen ambient," *J. Alloys Compd.*, vol. 694, pp. 1280–1286, Feb. 2017.

[36] Z. X. Mei *et al.*, "Growth of In_2O_3 single-crystalline film on sapphire (0001) substrate by molecular beam epitaxy," *J. Cryst. Growth*, vol. 289, no. 2, pp. 686–689, Apr. 2006.

[37] F. Zhang, K. Saito, T. Tanaka, M. Nishio, and Q. Guo, "Wide bandgap engineering of $(GaIn)_2O_3$ films," *Solid State Commun.*, vol. 186, no. Supplement C, pp. 28–31, May 2014.

[38] H.-U. Krebs *et al.*, "Pulsed Laser Deposition (PLD) -- A Versatile Thin Film Technique," in *Advances in Solid State Physics*, vol. 43, 2003, pp. 101–107.

[39] H. M. Smith and A. F. Turner, "Vacuum Deposited Thin Films Using a Ruby Laser," *Appl. Opt.*, vol. 4, no. 1, p. 147, Jan. 1965.

[40] D. Oka and T. Fukumura, “Crystal engineering for novel functionalities with oxide thin film epitaxy,” *CrystEngComm*, vol. 19, no. 16, pp. 2144–2162, Apr. 2017.

[41] C. B. Carter and M. G. Norton, *Ceramic Materials Science and Engineering*. Springer, New York, NY, 2007.

[42] M. Lee, *X-ray diffraction for materials research: from fundamentals to applications*. Oakville, ON : Boca Raton, FL: Apple Academic Press ; CRC Press, 2016.

[43] Y. Waseda, E. Matsubara, and K. Shinoda, *X-Ray Diffraction Crystallography*. Berlin, Heidelberg: Springer Berlin Heidelberg, 2011.

[44] P. Van der Heide, *X-ray photoelectron spectroscopy: an introduction to principles and practices*. Hoboken, N.J: Wiley-Blackwell, 2012.

[45] S. Hofmann, *Auger- and x-ray photoelectron spectroscopy in materials science: a user-oriented guide*. Berlin ; Heidelberg: Springer, 2013.

[46] W. Priyantha, G. Radhakrishnan, R. Droopad, and M. Passlack, “In-situ XPS and RHEED study of gallium oxide on GaAs deposition by molecular beam epitaxy,” *J. Cryst. Growth*, vol. 323, no. 1, pp. 103–106, May 2011.

[47] H. Fujiwara and H. Fukiwara, *Spectroscopic Ellipsometry: Principles and Applications*. New York, UNITED KINGDOM: John Wiley & Sons, Incorporated, 2007.

[48] H. G. Tompkins and J. N. Hilfiker, *Spectroscopic ellipsometry: practical application to thin film characterization*. New York, [New York] (222 East 46th Street, New York, NY 10017): Momentum Press, 2016.

[49] H. G. Tompkins, E. A. Irene, and ScienceDirect Freedom (Patron driven), Eds., *Handbook of ellipsometry*. Norwich, NY : Heidelberg, Germany: William Andrew Pub. ; Springer, 2005.

[50] H.-H. Perkampus, *UV-VIS Spectroscopy and Its Applications*. Berlin Heidelberg: Springer-Verlag, 1992.

[51] E. M. Secula, "Resistivity and Hall Measurements," *NIST*, 16-Apr-2010. [Online]. Available: https://www.nist.gov/pml/engineering-physics-division/popular-links/hall-effect/resistivity-and-hall-measurements. [Accessed: 04-Jul-2018].

[52] S. Grover, "Effect of Transmission Line Measurement (TLM) Geometry on Specific Contact Resistivity Determination," p. 112.

[53] H. von Wenckstern *et al.*, "Structural and optical properties of $(In,Ga)_2O_3$ thin films and characteristics of Schottky contacts thereon," *Semicond. Sci. Technol.*, vol. 30, no. 2, p. 024005, 2015.

[54] D. Splith *et al.*, "Determination of the mean and the homogeneous barrier height of Cu Schottky contacts on heteroepitaxial β-Ga_2O_3 thin films grown by pulsed laser deposition," *Phys. Status Solidi A*, vol. 211, no. 1, pp. 40–47, Jan. 2014.